

# Scattering of curvature radiation explains key geometric properties of radio pulsar signals

J. Dyks

*Nicolaus Copernicus Astronomical Center, Polish Academy of Sciences, Rabiańska 8, 87-100, Toruń, Poland*

Accepted .... Received ...; in original form 2020 Sep 22

## ABSTRACT

Radio pulsars exhibit multitude of inexplicable phenomena, in particular: average pulse profiles with core-cone structure and alternations of orthogonal polarization in time, frequency and pulse longitude. I show that the **conal morphology of radio profiles along with some aspects of frequency evolution and polarization can be explained** by the inverse Compton scattering of the curvature radiation. The conal morphology appears because the long-mean-free-path scattering in dipolar magnetosphere occurs at preferred directions even in medium of constant and uniform density. The narrowing of profiles **into boxy shapes** at high frequency results from shortening of the mean free path. The curvature radiation is **implied** on two independent grounds: it explains **some** details of circular polarization and its microbeam is directly observed as magnified bifurcated components (BCs). The latter are wide low-frequency microbeams upshifted in frequency with their width preserved by beam-copying scattering in divergent magnetic field. **Their large flux is partly caused by the compression of the full emitted spectrum into the narrow observed bandwidth.** The wide low-frequency microbeams can induce coherency in large magnetospheric volumes, which abates the energy budget by orders of magnitude. The scattering implies the negative O-mode ray interference which **allows us to interpret** the mode alternation in frequency and time. Described mechanisms open way to new interpretations in pulse modulation studies and have important practical implications for modelling of the polarization angle. **The properties of BCs imply that the observed radio flux is strongly affected by the scattering-driven blueshift and spectral compression.**

**Key words:** pulsars: general – pulsars: individual: PSR J1012+5307 – pulsars: individual: PSR B1451–68 (PSR J1456–6843) – pulsars: individual: PSR B1700–32 (PSR J1703–3241) – polarization – radiation mechanisms: non-thermal.

## 1 INTRODUCTION

Despite more than half a century of observations, and vast data collected for intensity profiles, polarization (Hankins & Rankin 2010; Stinebring et al. 1984; Noutsos et al. 2015; Tiburzi et al. 2013) and flux density modulation (Deshpande & Rankin 2001; Weltevrede et al. 2007), radiative pulsar properties have resisted most of interpretive efforts. The curvature radiation (CR) continues to be regarded as a likely emission process (Gangadhara 2010; Gil, Lyubarskii & Melikidze 2004; Luo & Melrose 1992; Mitra et al. 2009; Wang et al. 2015; Dyks et al. 2010, hereafter DRD10), despite it is not sufficiently energetic (Kaganovich & Lyubarsky 2010; Dyks & Rudak 2013) nor flexible to explain the observed signal geometry. The induced inverse Compton scattering (ICS) has **been identified as the mechanism that likely re-**

**shapes the emitted radiation** (Blandford & Scharlemann 1976; Lyubarskii & Petrova 1996). However, the scattering has been applied rather to extreme or peculiar phenomena (backward interpulses, nonbifurcated precursors, giant pulses, Petrova 2004, 2008a,b) and its role in shaping the regular profile morphology has not been recognized. **In this paper I show that pulsar signals contain several geometric signatures of scattering and CR.**

Average profiles of radio pulsars exhibit the mysterious nested cone morphology with the central component (core) surrounded by a pair or two pairs of conal components (Rankin 1983, 1993). Dipolar  $\vec{B}$  field offers little structure in the polar regions, therefore, since pulsar discovery in 1967, there has been only one dead-end interpretation proposed for the origin and size ratio of the cones (Wright 2003). The

present paper **offers different** origin of the conal morphology in Section 2.

Section 3 describes the key properties of coherent transitions between orthogonal polarization modes (OPMs) that are needed to understand the evolution of radio pulsar profiles with frequency and pulse longitude. The coherent OPM transition (COMT) is revealed by recent observations of strong circular polarization in B1451-68 (Dyks, Weltevrede & Ilie 2021, hereafter DWI21).

A self-consistent interpretation of a pulsar radio profile (B1700-32, Johnston et al. 2008, hereafter JKMG08) across a wide frequency range is described in Section 4, which **proposes** the origin of radius-to-frequency mapping (RFM). Implications for subpulse modulation studies (McSweeney et al. 2019; Maan 2019) are given in Section 5. Interpretations of subpulse modulations have so far mainly focused on the carousel model (Rudermann & Sutherland 1975; Gil et al. 2003; Deshpande & Rankin 2001). Surface oscillations (Clemens & Rosen 2004; 2008) have been proposed as an interesting alternative capable to explain the half-cycle jump in modulation phase (Edwards et al. 2003). In Section 5 I show that subpulse modulations **can also be interpreted** with the plasma-density-sensitive scattering and interference which occur within the radio beam itself.

Pulsars show strong circular polarization  $V$  which has been studied theoretically (Lyubarskii & Petrova 1998; Wang et al. 2000; Hakobyan et al. 2017; Galishnikova et al. 2020; Jones 2016; Melrose 2003) and empirically (Edwards & Stappers 2004; Melrose et al. 2006; Dyks 2017). In several pulsars (eg. PSR B1451-68, B1857-26, Ilie 2019) the polarization varies with pulse longitude in such way that the observed polarization state rotates meridionally on the Poincare sphere (P. sphere) and it is passing through the  $V$  pole at some stage (meridional circularization with the  $V$ -pole passage, Dyks 2020). In Section 6 I show that this meridional rotation **likely** results from the properties of the elementary emission pattern (microbeam) of the curvature radiation (CR).

In Section 7 I describe the origin of bifurcated components (BCs) observed in radio pulsar profiles. The excessive size of these components, and their similarity to the frequency-integrated CR microbeam will become clear and consistent with each other.

The explanations proposed **are related to** some long-standing problems, such as the origin of similar OPM amounts or the origin of subwavelength phase lags needed for the strong circular polarization. These subjects are also discussed below.

## 2 THE ORIGIN OF CONAL PROFILE MORPHOLOGY

**The observed cone size ratio indicates that** the cones correspond to different orders of scattering in the regime of a long mean free path (MFP). Consider a low-altitude core ray emitted tangentially to the local magnetic field, at the polar angle  $(3/2)\theta_{em}$ , where  $\theta_{em}$  is the colatitude of the emission point, located at a radial distance  $r_{em}$ . The ray propagates along the solid slanted line in Fig. 1. In the relativistic limit, the ray will be scattered along the local  $\vec{B}$  field (black vectors) at a scattering angle  $\theta_{sc}$  as

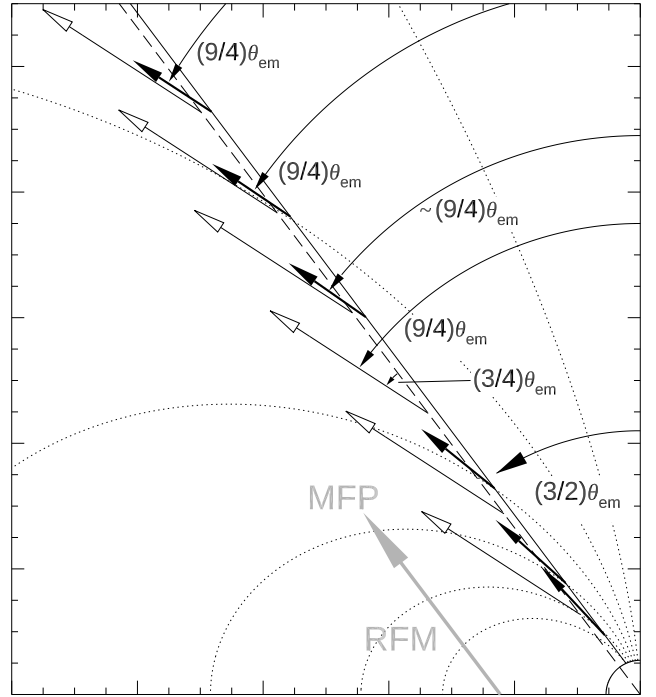


**Figure 1.** Formation of conal emission through scattering of low-altitude core rays that are emitted at  $(3/2)\theta_{em}$  and propagate upward along the near-diagonal solid line. The polar angle of the local  $B$ -field that they encounter (short black arrows) is quickly approaching  $(9/4)\theta_{em}$ . For any scattering altitude which is not close to the emission point, the emitted waves are scattered at this preferred angle, which produces a cone. White-tip arrows show the fixed local direction of  $\vec{B}$  along the dashed radial line which is parallel to the initial propagation direction. The low- $\nu$  profile widening is caused by the increase of the mean free path, as shown with the large grey arrow.

measured between the initial and scattered ray direction. Dipolar magnetic field along any radial line (including the dashed line parallel to the ray in Fig. 1) makes a fixed angle  $\theta_x$  with respect to the radial direction, as shown with the white tip arrows. The angle is equal to half of the radial line tilt, in this case:  $\theta_x = (3/4)\theta_{em}$ . The corresponding polar angle (measured from the dipole axis) is equal to  $(3/2)\theta_{em} + (3/4)\theta_{em} = (9/4)\theta_{em}$ , so it is larger by the factor 3/2 than the radial line tilt. Since the ray path is nearly radial far from  $r_{em}$ , the propagating ray is cutting the local  $\vec{B}$  field at an increasing angle which quickly approaches  $\theta_x$ . Only near the emission point, ie. for a short MFP  $\eta_{sc}$ , the scattering direction depends on  $\eta_{sc}$  or altitude. For nonlocal scatterings ( $\eta_{sc} \gg r_{em}$ ) all the rays are scattered at the same polar angle  $(9/4)\theta_{em}$ . This is the inner cone.

The reasoning of **previous paragraph** is recursive, so if the conditions allow for the second-order scatterings at long MFP, the outer cone is produced at the angle of  $(3/2)(9/4)\theta_{em} = (27/8)\theta_{em}$  (Fig. 2). The ratio of the inner to outer cone width is  $R_{io} = 2/3 = 0.66$ .

The observed cone size ratio has been estimated in a nearly model-independent way from the measurements of the component separations in Q and M profiles (Dyks & Pierbattista 2015, hereafter DP15). In that method, the peak-to-peak separations  $\Delta_{in}$  and  $\Delta_{out}$  are measured for

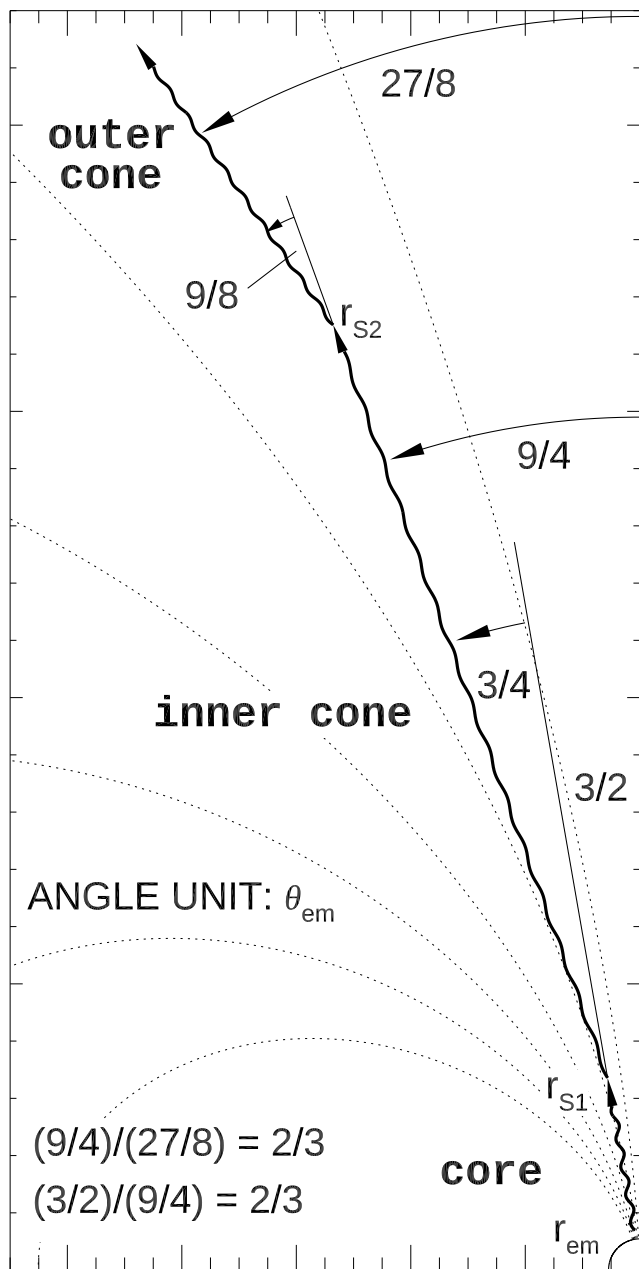


**Figure 2.** Relations between propagation angles in the core, inner cone and the outer cone rays. The unit of angle is the initial colatitude of an emission point  $\theta_{em}$  (arbitrary, but small). As explained in Fig. 1, the long mean free path and dipolar  $\vec{B}$  field ensure that beams of consecutive scattering orders are scaled by the factor of  $3/2$ . The inner to outer cone size ratio is thus equal to  $0.66$ .

the inner and outer pair of conal components and the ratio  $R_W = \Delta_{in}/\Delta_{out}$  is calculated. The value of  $R_W$  only depends on the distance from the beam centre (called impact angle) at which the sightline is cutting the beam. The upper limit in the  $R_W$  distribution corresponds to the central sightline traverse through the beam (see fig. 1 in DP15). As shown in fig. 4c and table 1 in DP15, ten percent of all the Q and M pulsars have the highest  $R_W$  value of  $0.63$  which confirms the scattering origin. The number of pulsars

with near-maximum  $R_W$  is much lower than predicted for a conal structure, however, this can result from the beam suppression in the central-traverse region, as observed for the **interpulse** of PSR J1906+0746 (Desvignes et al. 2019).

Another estimate of observed  $R_{io}$  is larger ( $\sim 0.75$ , Rankin 1993; Mitra & Deshpande 1999; Kramer et al. 1994), however, it was derived with indirect methods that use the curve of polarization angle (PA). As shown below (Section 3), the curve is usually distorted by either the scattering or the coherent OPM superposition.

Dipolar magnetic field geometry implies that for long  $\eta_{sc}$ , the scattering angle does not depend on scattering radii (Fig. 3, left) so the cones tend to appear readily. Since all scattering angles are proportional to  $\theta_{em}$ , essentially the cones are reflected version of the core (Fig. 3). This explains the usually-similar width scale of observed core and cone components.

In the above-described version, the model assumes multiple scatterings. The scattering MFP depends on the mode of scattering (resonant/nonresonant, spontaneous/induced), the geometry of scattering and other parameters (plasma density  $\rho$ ,  $B$ -field strength, scattering electron energy  $\gamma$ , observed radio wave frequency  $\nu_{obs}$ ). The estimate of MFP is complex, however, considerable optical depths have been found at least for the induced scattering (Blandford & Scharlemann 1976; Lyubarskii & Petrova 1996). Petrova (2008a) has shown that efficient induced scattering occurs within the polar tube provided that the emitted radiation has been amplified to the observed flux densities. Most of the incident flux can thus be displaced from the incident to a scattered beam. This way a redirected new incident beam is formed within the polar tube, with similar flux density as the original beam. The radio frequency is changed in the scattering by the factor  $\gamma^2\theta^2$ , where  $\theta$  is the angle between the incident ray and electron velocity. Therefore, multiple scatterings can be expected as soon as the radio and electron spectra are sufficiently wide and flat to ensure that the finally scattered frequency is equal to  $\nu_{obs}$ .

In a case without the multiple scatterings, a version of the model is possible in which the inner cone is formed by rays emitted near the last open lines (the emission is considered as the zeroth scattering order). Then the rays produced by the single (first) scattering must be identified as the outer cone. However, the observed core component then requires a separate justification, see also Sect. 4.1.2.

To interpret the frequency evolution of profiles, it is necessary to employ the properties of coherent OPM superposition at variable mode ratio and fixed phase lag.

### 3 COHERENT ORTHOGONAL POLARIZATION MODE TRANSITION

The coherent superposition of modal waves in general involves the effect of variable phase lag and variable mode amplitude ratio. The latter effect is crucial both in the pulse

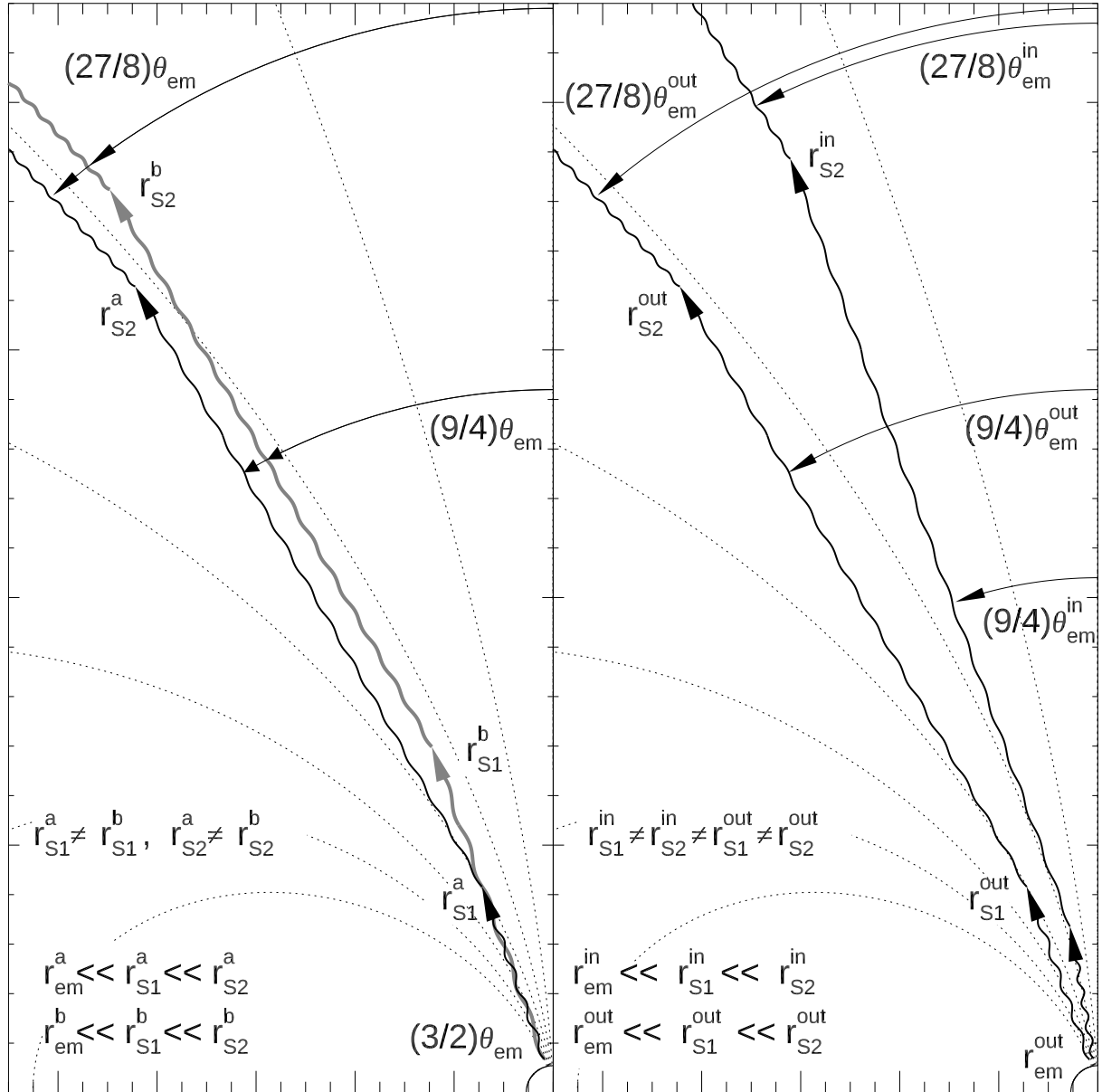


**Figure 3.** Geometry of long-MFP scattering for a pair of rays. Left: Two rays, ‘a’ (black) and ‘b’ (grey), emitted at the same polar angle  $(3/2)\theta_{em}$ . In spite of different scattering altitudes, the scattered rays of a given order propagate at the same polar angles, as shown with the double-tip arrows. Right: Two rays (inner and outer) emitted at different polar angles  $(3/2)\theta_{em}^{in}$  and  $(3/2)\theta_{em}^{out}$ . In each scattering order, the propagation directions of scattered rays preserve the initial angle ratio  $\theta_{em}^{in}/\theta_{em}^{out}$ .

longitude and frequency space, and will be discussed first, as the main subject of this section.

### 3.1 Mode-ratio governed coherent OPM transition

Consider two orthogonal and linearly polarized sinusoidal waves  $\vec{E}_X = \vec{E}_X \cos(\omega t - kz)$  and  $\vec{E}_O = \vec{E}_O \cos(\omega t - kz - \delta_{ox})$  that represent the proper modes X and O. Coherent superposition of the waves does not lead to depolarization, i.e. the total polarization fraction  $I_{pol}/I$  is constant and equal to 100%. The reason for this is elementary: a sum of the two vectors produces another vector with unique polarization state. The relative amount of the

linear and circular polarization, however, depends on the phase lag  $\delta_{ox}$  between the superposed modal waves. During the coherent OPM transition, the relative amplitudes of the modes change so that one mode (say X) initially dominates, then becomes negligible in comparison to the O mode. This can be parametrized by the increase of the mixing angle  $\tan \psi_{mx} = E_X/E_O$ . The geometry of the transition on the P. sphere is shown in Fig. 4.

If the lag  $\delta_{ox}$  between the O and X mode has the zero value, the total polarization stays 100% linear and the mixed (coherently summed) polarization state follows the thick part of the QU equator. When the modes are equal, the PA is passing through the  $45^\circ$  value at point A on the sphere (PA is equal to half the azimuth). **This** increase of PA, as

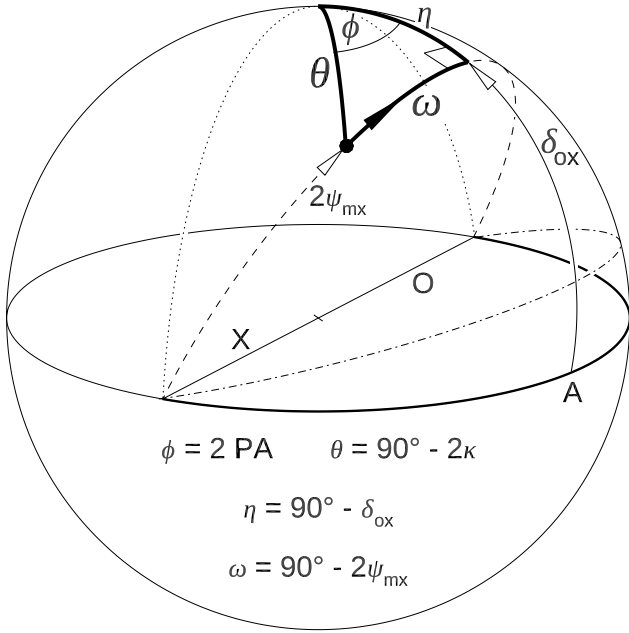


**Figure 4.** Mode-ratio driven coherent OPM transition on the P. sphere. Unlike in the case of the retardation, the observed polarization state (bullet) rotates across the direction of increasing lag  $\delta_{\text{ox}}$  (white-tip arrow on the right). The state rotates in the plane that contains the proper modes X and O and is coinciding with the modes at the QU equator. Depending on  $\delta_{\text{ox}}$ , the observed polarization state follows the dotted, thin solid, dot-dashed or the thick solid equatorial path between the X and O mode. Because the mode superposition is coherent, the signal never becomes depolarized. For  $\delta_{\text{ox}} \sim 90^\circ$  the state is passing near the V pole (observed as high  $V/L$  and stairs shaped PA curve). For  $\delta_{\text{ox}} \sim n180^\circ$  the coherent OPM transition only causes the continuous change of PA.

caused by the changing mode ratio (increasing  $\psi_{\text{mx}}$ ) can be directly observed with no distortion **that would otherwise arise from the off-equatorial motion of the pol. state.** This mode transition is extremely difficult to notice in pulsar data: no polarization fraction (whether the total  $I_{\text{pol}}/I$ , linear  $L/I$  or circular  $V/I$ ) reveals any OPM jump. Worse yet, the OPM jump can be mistaken with the rotating vector model (RM), because the PA can change with pulse longitude  $\Phi$  essentially in the same way as in the RVM case (see below).

If  $\delta_{\text{ox}} \sim 90^\circ$ , the polarization state moves upward meridionally, following the dotted meridian in Fig. 4. Note that the PA stays constant at the X mode value until the V pole is passed by – at this moment the PA quickly changes by  $90^\circ$  (azimuth by  $180^\circ$ ). This sudden OPM transition has been described as the V-pole-passage-driven OPM jump (VPP OPM jump, Dyks 2020). Since the scattering into cones mostly redirects the O-mode, the VPP OPM transition tends to occur on both sides of the core (PSR B1451-68, DWI21; PSR B1857-26, Mitra & Rankin 2008; PSR B1237+25, Smith et al. 2013). Depending on which side are the V poles passed by the polarization state, the PA curve **can become stairs-shaped** (two upward OPM jumps, or two downward jumps), U-shaped (downward and upward OPM jump) or it can have an inversed-U shape (transition

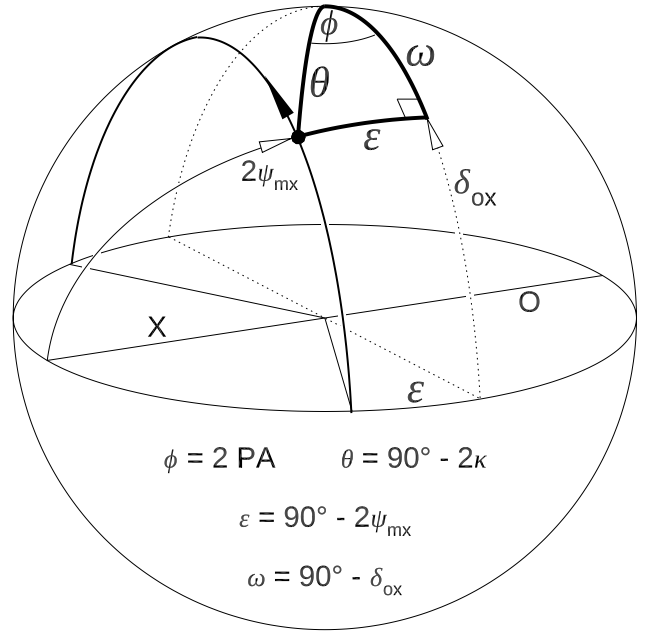


**Figure 5.** Retardation-driven rotation of polarization state on the P. sphere. The state (bullet) does not have to follow a great circle and does not coincide with the proper modes (X and O).  $\delta_{\text{ox}}$  is the OX phase lag, and  $\psi_{\text{mx}}$  is the mixing angle which sets the mode ratio.

up and down). Hereafter, all these forms will be referred to as ‘stairs-shaped PA curves’. Since  $L/I$  corresponds to the projection of a polarization state vector on the QU plane, the values of  $L/I$  and  $|V|/I$  are anticorrelated in the coherent OPM transition. Therefore, this quarter-wave-lag type of OPM jump can be recognized by the maxima of  $|V|/I$  coincident with minima of  $L/I$  and with the steep parts of the stairs-like PA curve. All the details are observed in the below-discussed PSR B1700-32 at 1.4 GHz (second panel from bottom in Fig. 6) which demonstrates that coherent OPM transitions occur as a function of longitude in this object (though the polarization state must be passing at a further distance from the V-pole to keep  $L/I > |V|/I$ , see below). Note that for an incoherent mode superposition,  $L/I$  at OPM jumps should coincide with minima of  $|V|/I$  which is not the case in B1700-32.

### 3.1.1 Comparison to the retardation-driven OPM jump

The mode-ratio driven OPM jump (ie. occurring at a fixed  $\delta_{\text{ox}}$ ) is completely different from a retardation-driven near-OPM transition that is caused by the increase of the O-mode lag (Fig. 5). In the retardation-driven OPM jump the polarization state rotates in the plane orthogonal to the OX proper mode axis. The state never coincides with the proper modes (it is always a mixed state) and the jump is orthogonal only for equal mode amplitudes ( $\varepsilon = 0$  in Fig. 5). This type of retardation-driven effect may also be observed in radio pulsars (PSR B0329+54, Edwards & Stappers 2004, see, however, Melrose et al. 2006). As found in DWI21, the coherent mode-ratio-driven OPM transition can be discerned from the retardation-driven jump, based on compactness of the observed polarization state distribution near the QU

equator. In the case of the mode-ratio-driven OPM jump the patches of flux on the P. sphere become blurred beyond the QU equator, where they are no longer pure (proper) polarization states.

### 3.2 Distortions and displacements of PA tracks

As shown in DWI21, variations of the PA during coherent OPM transitions (COMTs), whether driven by the retardation or the mode ratio change, follow essentially the same curve as the RVM.

In the case of linear proper modes, the motion of the bullet shown in Fig. 4 is described by the equation for the polarization angle  $\psi$ :

$$\tan(2\psi) = \frac{\tan(2\psi_{\text{mx}} - 90^\circ)}{\cos \delta_{\text{ox}}} \quad (1)$$

and for the ellipticity angle  $\kappa$ :

$$\sin(2\kappa) = \sin(2\psi_{\text{mx}}) \sin \delta_{\text{ox}}. \quad (2)$$

Equation (1) is nearly the same as the RVM with dipole tilt  $\alpha = 90^\circ$  and the viewing angle  $\zeta = \delta_{\text{ox}}$ :

$$\tan(\psi_{\text{RVM}}) = \frac{\tan(\Phi - \Phi_0)}{\cos \zeta} \quad (3)$$

(cases of more general motion on the P. sphere are discussed in DWI21).

Therefore, coherent OPMs easily go unnoticed in radio pulsar data. The quarter-wave COMTs can be identified through their high  $|V|/I$  and DWI21 describe several cases where the COMTs are misinterpreted as RVM. However, at frequencies where  $\delta_{\text{ox}} \sim n180^\circ$  (motion within the QU equator), the COMTs only cause gradual change of the PA value and are very difficult to notice. If the lag distribution is not precisely centered at this half-wave value, (dashed or dot-dashed path in Fig. 4), the coherent mode transitions produce the PA curve with the shape of stairs with slanted treads (B1703 at 1.4 GHz, second from bottom panel in Fig. 6; B1913+16, Weisberg & Taylor (2020), see fig. 1 in Dyks 2017).

Since  $\delta_{\text{ox}}$  depends on the frequency  $\nu$ , the clear stairs-shaped distortions of the PA curve appear whenever  $\delta_{\text{ox}}(\nu) \sim \pi/2 + n\pi$ . In such case the flat parts of the PA curve correspond to the orientation of the  $\vec{B}$  field in the birefringent propagation region and do not follow the low- $r$  RVM.

As will be discussed below, the flat outer parts of PA tracks at the frequencies where the profiles exhibit the conal structure cannot be used for the RVM fitting either. This is because the outer track parts are made flat by the scattering (the inner PA values are moved to profile periphery).

As also discussed below, the scattering **opens the possibility of** interference which may cause alternation of OPMs in frequency. The resulting vertical displacements of the entire PA track may affect the rotation measure determination (Ng et al. 2020). The mode alternation also affects the question of which polarization mode is aligned with the proper motion direction (Johnston et al. 2005).

## 4 FREQUENCY EVOLUTION OF PROFILES

The ICS enables interference of scattered waves and mode alternation caused by the cancelling of the superposed waves. Moreover, the coherent mode superposition allows for existence of OPM transitions where they have previously seemed excluded by lack of their signature in polarized fractions. These features make it possible to interpret the frequency evolution of polarized profiles.

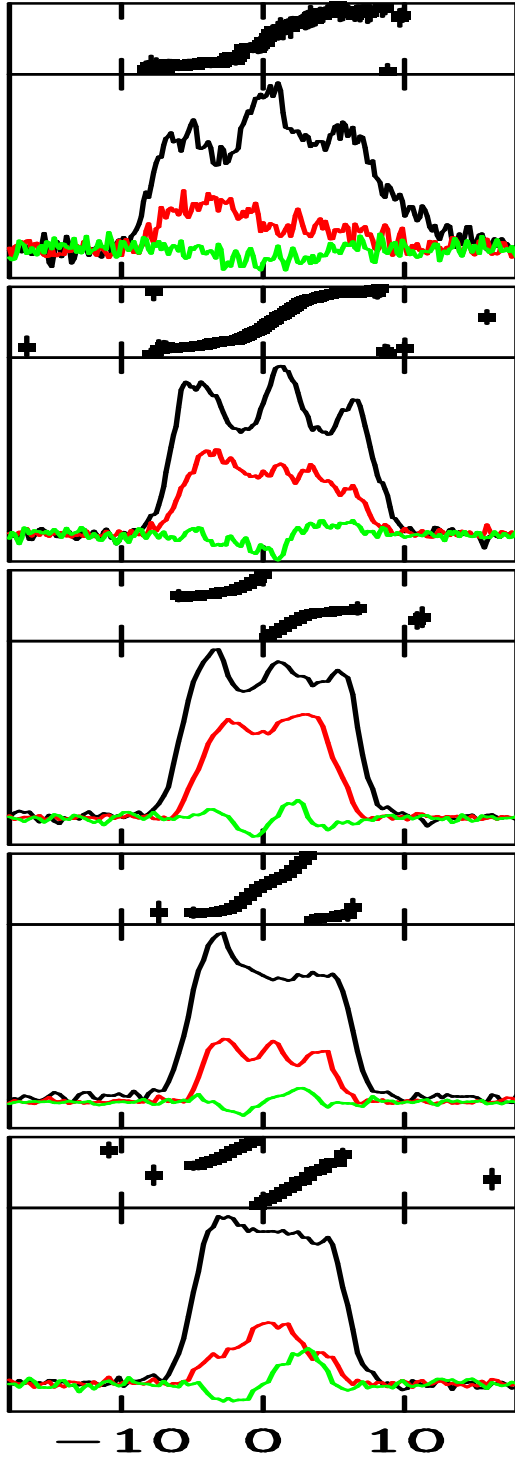
### 4.1 Interpretation of a radio pulse profile in frequency and longitude

Fig. 6 shows the  $\nu$  evolution for PSR B1700-32, as observed by Parkes Telescope and GMRT (JKMG08). The main discussed effects that shape this ‘beautiful example of a triple profile’ are shown in Fig. 7. The lowest- $\nu$  stage (panel a) is not observed in B1700-32, but is often seen in other pulsars: the sinusoid-like  $V$  under the narrow core is consistent with the convolution of CR microbeams (Michel 1991, p. 356) while the central PA curve may reflect the rotating vector model (RVM). With increasing  $\nu$  the profile develops weak separated conal components, ie.  $\eta_{\text{sc}}$  is large but decreasing. At 322 MHz (panel b) scatterings at a smaller angle fill in the beam. The transport of flux towards the profile peripheries makes the PA curve flat: the outer parts do not correspond to the RVM. The peripheric PA just consists of inner PA values that have been relocated outwards by the scattering.<sup>1</sup> **This effect explains the notorious problems with the RVM fitting of flat outer parts of PA curves (eg. PSR B1857–26, Mitra & Rankin 2008).** At 690 MHz the ICS MFP is shorter for most rays, which makes the profile narrower (the rays are less defocused by the scattering, see black arrows in Fig. 1).

A new effect ( $\text{MA}_\nu$ , **for mode alternation in the frequency space**), which is observed between 0.69 and 1.4 GHz, is the vertical displacement of the entire PA curve by  $90^\circ$ . As was explained in Section 3, **this can be interpreted as a coherent transition between the orthogonal polarization modes (OPMs) that occurs in the frequency space.** In the coherent case, the inversion of OPM ratio leaves no trace in total polarized fraction ( $I_{\text{pol}}/I$ ) and can leave no or little trace in the linear fraction  $L/I$  or the circular  $V/I$ . **The scattering implies differences of geometric paths with possible interference between** different scattered (or scattered and unscattered) O-mode rays. **This may lead to the swapping of OPMs.**<sup>2</sup> The O-mode interference occurs at a phase lag  $\delta_{\text{oo}}(\nu, \Phi)$  which depends on the frequency  $\nu$  and the pulse longitude  $\Phi$ . The  $\Phi$  dependence appears because waves scattered at larger angles  $\theta_{\text{sc}}$  travel a longer geometric path. In the absence of strong corotational asymmetry,  $\delta_{\text{oo}}(\Phi)$  is expected to increase with distance from the profile center. The  $\nu$  dependence results from the change of the wavelength itself. Depending on  $\nu$ , the O-mode rays **can** interfere positively ( $\delta_{\text{oo}} \sim n2\pi$ ) or negatively ( $\delta_{\text{oo}} \sim \pi + n2\pi$ ), which causes that either the total O mode or the X mode

<sup>1</sup> This intramagnetospheric PA flattening is different from the interstellar effect discussed in Karastergiou (2009).

<sup>2</sup> **The scattering may also lead to interference through spectral compression of the emitted spectrum at the observed  $\nu$ , see Sect. 7.2.**



**Figure 6.** Frequency evolution of the polarized profile of PSR B1700-32 (fig. 4 in Johnston et al. 2008). From top to bottom, the frequencies are: 243 and 322 MHz (GMRT) and 0.69, 1.4 and 3.1 GHz (Parkes Telescope). The PA at the Parkes frequencies is calibrated in absolute way. The range of PA axis is  $(-90^\circ, 90^\circ)$ , the longitude is in degrees. Note the stairs-shaped PA at 1.4 GHz, the orthogonal displacements of PA with  $\nu$ , and the emergence of conals with flat PA.

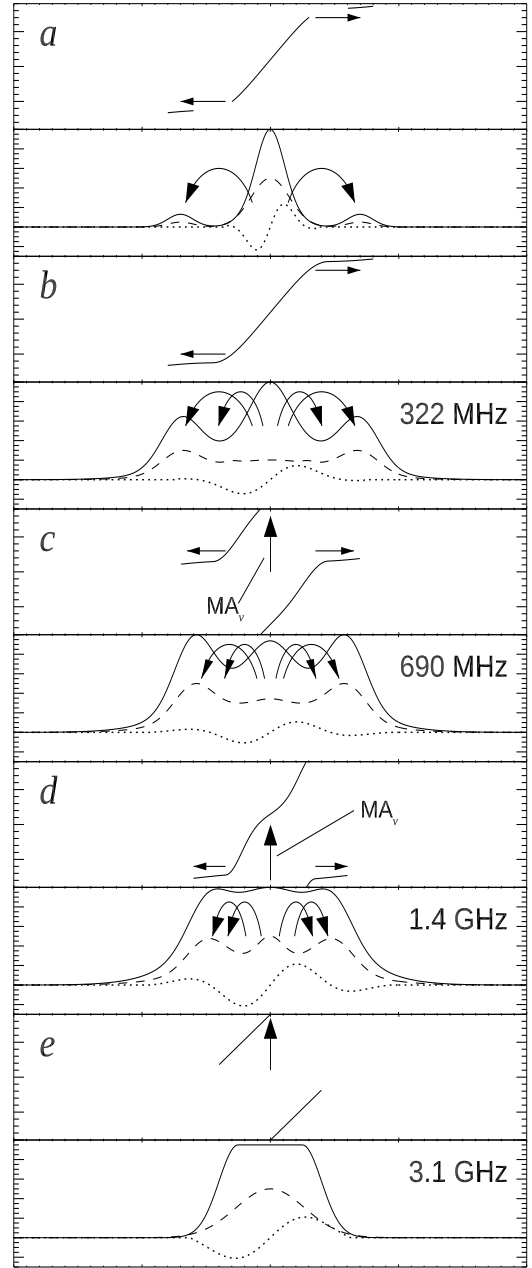


**Figure 7.** Frequency evolution of the polarized profile of PSR B1700-32 (interpretation of Fig. 6). Bent arrows show the ray displacement by the scattering. The vertical arrows (denoted  $MA_\nu$ ) show the orthogonal mode alternation with frequency, i.e. the orthogonal displacements of the PA curves, that may be interpreted by interference. Horizontal arrows show the scattering-induced flattening of the peripheric PA curves.

dominates in the signal. Therefore, the PA curve exhibits the  $MA_\nu$  at least one more time between 1.4 and 3.1 GHz (the Parkes PA is calibrated in the absolute way, JKMG08). Since the  $\nu$  change applies for all longitudes, the entire PA curve **may be** vertically translated, regardless of whether the O or X mode dominates at a given  $\Phi$ . **This happens when the X and  $\nu$ -averaged O mode have similar strength: then the X mode appears at pulse longitudes with negative interference (NI) whereas the**

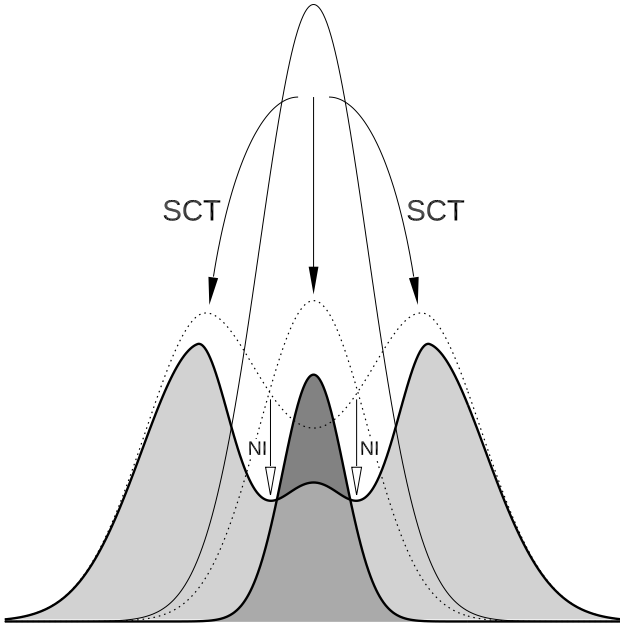


**Figure 8.** Key mechanisms of conal profile formation. The scattering (SCT) is redirecting the core emission into the wider emission component shown with the dotted line. This also makes the core less bright (also shown with dotted line). The negative interference (NI) between the scattered and emitted rays **may furthermore suppress** the emission on both sides of the core. The observed grey components are thus a coherent sum of the dotted components.

#### O mode at longitudes of positive interference (PI).

At 1.4 GHz the PA curve assumes a stairs-like shape, which appears because at this  $\nu$  the phase lag  $\delta_{xo}$  between the total O and X modes is closer to the quarter-wave value. Thus, at this  $\nu$ , with increasing longitude  $\Phi$  the observed polarization state rotates non-equatorially on the P. sphere. Just as in the frequency space, despite dominant OPMs swap in longitude, there is no trace of this in polarized fractions, since the OPM jumps are coherent.

#### 4.1.1 The origin of radius-to-frequency mapping

At 3.1 GHz (Figs. 6 and 7) the scatterings occur in the short MFP limit, ie. in the bottom right corner of Fig. 1. The small profile width corresponds to the local low-altitude scatterings. Thus, the radius-to-frequency mapping (RFM) is caused by the changes of the scattering MFP: at high  $\nu$  the value of  $\eta_{sc}$  is short which is erasing the  $(1.5\theta)$ -direction preference and fills in the polar tube at the scattering altitude, thus producing the narrow boxy profiles.

Pulsar profiles are thus dominated by the scattering-driven ray reflection **with possible interference, which may lead to** the  $\nu$ -dependent mode alternation ( $MA_\nu$ ) (see Fig. 8). The cones are indeed produced at a higher altitude than the core, which has different radio spectrum, because it is made of unscattered rays and rays produced by small-angle scatterings.

#### 4.1.2 Emission from neighbouring colatitudes

The scattering at the angle of  $(3/2)\theta_{em}$  produces a hollow cone only when the emission from neighbouring  $\theta_{em}$  does not fill in the cone. A particular value of  $\theta_{em}$  must therefore be justified for the innermost cone. Since the core is sometimes observed bifurcated, one may argue that the core emission is strongest near the last open field lines, thus selecting the special  $\theta_{em}$ . Another possibility is that the core beam is essentially filled in, and the hollowness of the inner cone results from the scattering rate, which in general increases with the collision angle (both for the spontaneous and induced case, Petrova 2008a). This way the sides of the core would be scattered much more efficiently than the center. This is the reason for which the dotted scattered component is plotted with the central minimum in Fig. 8, even before any interference effects are considered. It is also worth to note that even a cone without any hollowness (eg. a low wide rectangle), if superposed on a narrow core emission (a tall narrow rectangle), would be classified as a ‘core plus cone’ structure. Therefore, it is valid to conclude that even a uniform and constant charge density distribution can produce conally-structured average profiles (which change with  $\nu$ ).

## 5 TIME MODULATION

This section shows that in the presence of magnetospheric density fluctuations, the scattering with  $MA_\nu$  becomes a **promising** scenario for interpreting the time modulation phenomena. **The below-discussed model ignores any lateral structure within the polar tube, so it should be considered as an opposite limiting case to the laterally-structured models such as the carousel of sparks.**

When the magnetospheric plasma density  $\rho$  is fluctuating at a period  $P_\rho$ , the profile will undergo periodic and somewhat discrete reshaping, as shown in Fig. 9. The core emission is produced during a low- $\rho$  state (left, dashed arrows), the inner cone (IC, middle, dotted arrows) appears when  $\rho$  allows for the first order scatterings, and the outer cone (OC, right, solid arrows) is created in the most dense state. A pulsar may go through all the stages (core, IC, OC) which can produce the M type profiles, or just two stages (core/IC or IC/OC) which can produce the triple (T) or quadruple (Q) types as defined by Rankin (1983). The look of profiles furthermore depends on the usual detectability conditions: some stages may be missed by the line of sight, because the phase of sampling depends on the commensurability of  $P_\rho$  and the star spin period. If an observation is short, the exact time when it was done is also important. **However, the most important factor affecting the appearance of the subpulse may be the condition to upscatter the emitted radio spectrum to the observed band (see Sect. 7).**

Transitions between the outer (conal) emission and the inner (core/IC) emission have been observed in the modulation patterns of pulsars, for example in PSR B1237+25

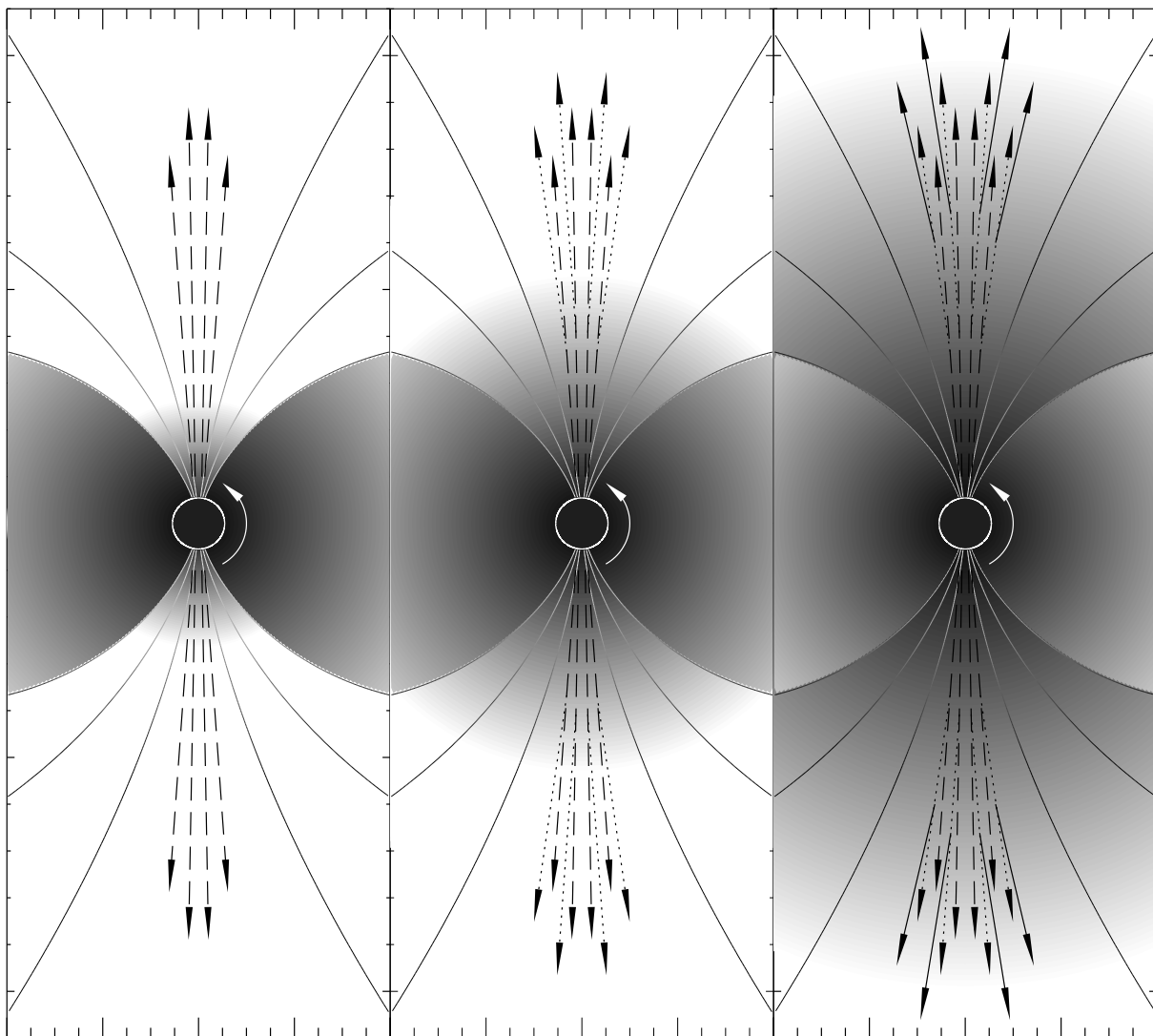


**Figure 9.** Influence of magnetospheric plasma oscillations (shown at three different phases) on the emitted radio beam. Left: low density phase with unscattered core emission (dashed rays). Middle: medium density phase with scattering of inner cone rays (dotted). Right: high density phase with two orders of scattering producing both cones. The solid outer cone rays are shown without scale. To preserve the  $3/2$  beam size ratio,  $\eta_{sc}$  must be large compared to  $r_{sc}$ .

(Srostlik & Rankin 2005). In one modulation mode of this pulsar, the activity of components follows a special order: (1, 5, 2, 4, 3), which has been interpreted as the spiraling motion (Hankins & Wright 1980). The transitions from the outer to inner components are consistent with Fig. 9, whereas the particular ordering of components can be explained as the rotation-induced scattering asymmetry between the leading and trailing side of the polar tube (see Fig. 10). Because of the rotation, the scattering angles, which affect the rate of scattering, are different on the leading and trailing side. The scatterings then occur at different altitudes on each side, thus at a different phase of the density fluctuation cycle.

A half-cycle jump has been observed in the modulation phase of PSR B0320+39 (Edwards et al. 2003), which led to formulation of a model based on star surface oscillations (Clemens & Rosen 2004; 2008). With the observed OPM ratio influenced by either the negative interference (NI) or

positive interference (PI), the jump can arise directly in the radiated beam. The phase lag  $\delta_{oo}$  between the superposed rays, depends not only on  $\nu$ , but also on the pulse longitude  $\Phi$ , because larger scattering angles imply longer geometric paths. Therefore, longitudes dominated by the X mode (NI) can be separated from those dominated by the O mode (PI). Moreover, the phase lag  $\delta_{oo}$  depends on  $\rho$ , because the scattering MFP is shorter in denser medium, which implies different geometric paths and different phase lags  $\delta_{oo}(\rho)$ . If at some fluctuation stage the  $\rho$ -dependent  $\delta_{oo}$  is cancelling the O mode within the NI longitudes, it is also amplifying the O mode within the PI longitudes. For different  $\delta_{oo}(\rho)$  the cancelling/amplifying longitude intervals will be swapped. This produces the  $MA_\nu$  with the half-cycle jump.

The drift pattern observed in PSR B0826-34 (Esamdin et al. 2005; Gupta et al. 2004) consists of thirteen similar (and quite lively) subpulses, which can also be interpreted as the  $\rho$ -sensitive maxima in the function  $I(\delta_{oo}(\nu, \Phi, \rho))$ . The

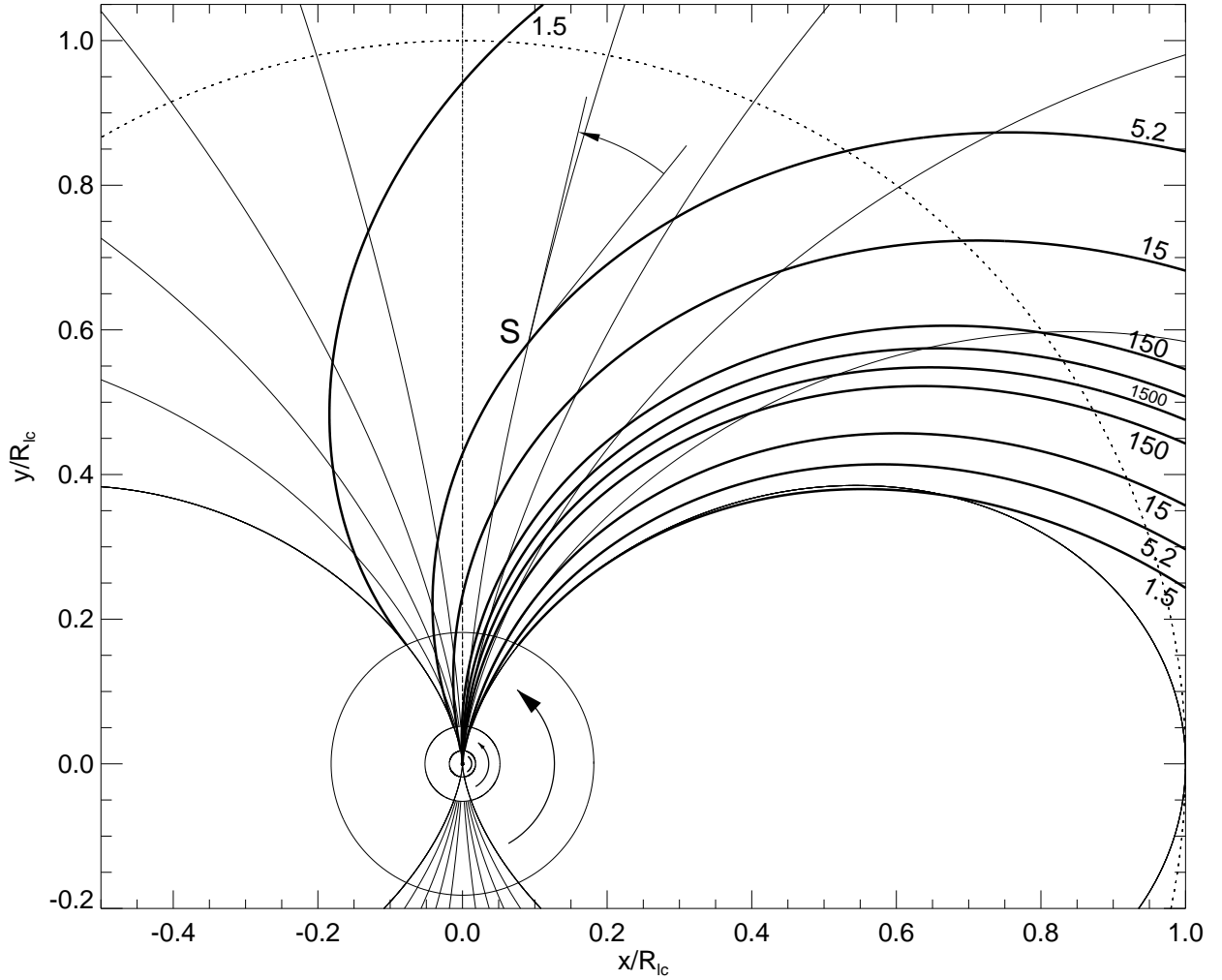


**Figure 10.** Photon trajectories in the rotating pulsar magnetosphere. Pairs of rays emitted tangentially to  $\vec{B}$  at the leading and trailing side of polar cap are shown in the plane of rotational equator for different rotation periods given in milliseconds. The star’s magnetic dipole is orthogonal to the rotation axis which is orthogonal to the page. The scattering angle is much larger on the leading side (eg. at point S) than on the trailing side. For long periods, the dipole axis moves out of the upward-propagating beams.  $R_{lc}$  is the radius of the light cylinder (dotted line).

periodic character of the NI cancelling is consistent with the similarity of the observed subpulses. The lively displacement of these features with time appears consistent with the  $\rho$ -dependent origin.

The model based on the scattering is also consistent with the sporadic appearance of core emission in D type pulsars (Young & Rankin 2012). These objects also exhibit the  $\nu$ -dependent  $MA_\nu$  (though not mentioned in Young & Rankin 2012, the  $MA_\nu$  can be seen in their figures; cf. fig. 3 in Dyks 2019).

The above-described modulation examples were selected because of their notoriously problematic character. With the magnetospheric fluctuations, scattering, and possibly interference, they can be interpreted naturally which shows large potential of the fluctuation-based model for pulsar modulations. Nevertheless, the fluctuations do not preclude a rotating lateral structure, which may be required in a full model capable of explaining the observed diversity of modulation.

Furthermore, the scattering inevitably involves the shifts of the emitted radio spectrum in frequency space. The invisible low- $\nu$  radio spectrum ( $\nu < 100$  MHz) can be ‘blueshifted’ into the observed frequency band (around 1 GHz), which makes the subpulses visible. A model is then possible, in which the oscillations of the plasma density (Fig. 9) are supplemented or replaced with the fluctuations of the energy distribution of scattering electrons. In such model it is the fluctuation of the electron energy spectrum which mainly drives the modulation phenomena, ie. the fluctuations operate in the frequency domain.

## 6 TYPE OF EMITTED RADIATION: POLARIZATION MODEL FOR B1451-68

The polarization state observed in a few pulsars (eg. PSR B1451–68, B1857–26, Ilie 2019) rotates meridionally on the P. sphere while our sightline is passing through the average profile. This can be clearly seen when the data are shown on the P. sphere, however, the circularization can also be studied when the usual PA-longitude plots are supplemented with figures showing the ellipticity angle  $\kappa$  (figs. 1, 2 in DWI21). The angle  $\kappa$  is defined as half the latitude measured from the QU equator. The polarization state observed at a given longitude in different periods can change in time to produce, eg., the alternating bands of orthogonal polarization. For fortunate commensurability of modulation and spin periods, however, the modal bands can be allocated to separate components (PSR B1451-68, DWI21; B1604-00, Rankin 1988). In such case the spread of states observed at a given altitude is narrow, and different states from different periods can form a **confined** patch of flux on the P. sphere. The patch center represents the typical polarization state at a given  $\Phi$  (hereafter also called a ‘state’ for short).

Within the pulse window of PSR B1451-68 (also in B1857-26) the polarization state makes one full rotation, visiting the states, **say**, X,+V,O,-V,X while the sightline is passing through the pulse profile. This forms zigzag-shaped variations of ellipticity angle  $\kappa$ , which increases to  $+45^\circ$  at the +V pole, then decreases to  $-45^\circ$  at the -V pole (fig. 1f in DWI21). The 1.4 GHz profile of B1451-68 is a barely resolved triple with a roughly triangular outline. **This suggests the profile is weakly affected by the scattering.** On both sides of the core peak, the polarization state is passing near each V pole, while continuing the always same-wise (say clockwise) rotation on the P. sphere. It has been shown for B1451-68 (DWI21) that the rotation is not caused by the O mode retardation - instead it represents two subsequent coherent OPM transitions (**say**, from X to O to X), each on either side of core. The cones and core thus have orthogonal polarization (which in other pulsars is observed as the orthogonally-alternating modulation pattern). To produce the monotonic rotation on P. sphere, the phase lag between the X and O waves in the neighboring components must change monotonically through the profile, having the values of, say,  $-90^\circ$  (leading conal),  $0^\circ$  (core), and  $+90^\circ$  (trailing conal).

Let us consider the curvature radiation (CR) as the process responsible for the polarization. If unscattered, an observed profile is a convolution of narrow slightly bifurcated curvature microbeams. If the profile is single peaked (as in B1451-68 at 1.4 GHz) there is a one-to-one correspondence between the profile side and the CR microbeam side (see Fig. 11). Namely, the leading side of the profile is dominated by the leading side of the microbeam, **and the trailing profile side by the trailing microbeam side.**<sup>3</sup> Thus, **if propagation effects are neglected**, the polar-

<sup>3</sup> If the emissivity primarily decreases with  $\theta_{em}$  (rather than with the magnetic azimuth  $\phi_m$ ), an opposite association is also possible and natural: the leading profile side corresponds to the trailing microbeam side (and vice versa) but this issue is not important for the present considerations.

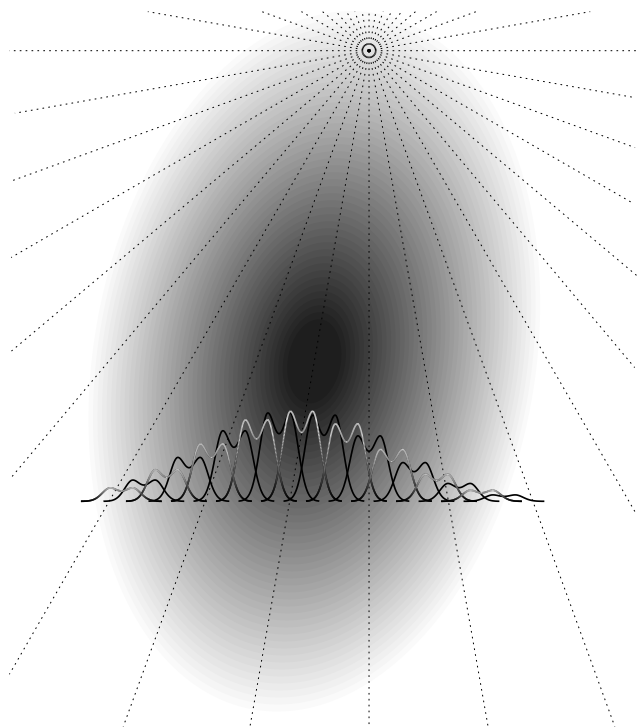


**Figure 11.** Convolution of CR microbeams in a single-peaked pulsar profile. Numerous microbeams (every second one with a whitish top) are shown as sampled by the line of sight passing horizontally across the grey beam. Because of the spatial emissivity gradient, the polarization of the CR microbeam survives in the average profiles: on the left side, at a longitude  $\Phi_{L0}$ , nearby right-hand side microbeams (at  $\Phi_L \gtrsim \Phi_{L0}$ ) contribute more flux than neighboring microbeams on the left side ( $\Phi_L \lesssim \Phi_{L0}$ ). This stronger flux comes from the left side of the adjacent right-hand side microbeams (some complexity caused by the central dip in the microbeam is ignored).

ization of the CR microbeam can be considered as a good representation of the polarization in the average profile. This reasoning justifies the view that the sinusoid  $V$  profile of core components corresponds to the similar sinusoid  $V$  profile in the elementary CR microbeam (Michel 1991). Periodic modulations, like subpulse drift bands, are not detected in B1451-68, so they can be ignored.

The vacuum CR microbeam is linearly polarized in the middle, but it has opposite circular polarizations in the wings (Sokolov & Ternov 1968; also see fig. 8.1 in Michel 1991). This is shown on top of Fig. 12 with the grey polarization ellipses. Therefore, when the microbeam is cut by the sightline, the polarization state moves only by a half meridian on the P. sphere, say from +V, through O, to -V. However, if the O mode is suppressed for whatever reason (eg. by the Landau damping or by the scattering-driven NI) the grey polarization ellipses are vertically compressed to the black ellipses that are shown below. This provides the full rotation observed in pulsar profiles (X,+V,O,-V,X).

As shown in bottom part of Fig. 12, the same conclusion can be expressed in the language of phase lag between the X and O modes: in the presence of birefringence, the ellipses are resolved into orthogonal O and X oscillations, ie. vertical and horizontal in the figure. The opposite handedness of

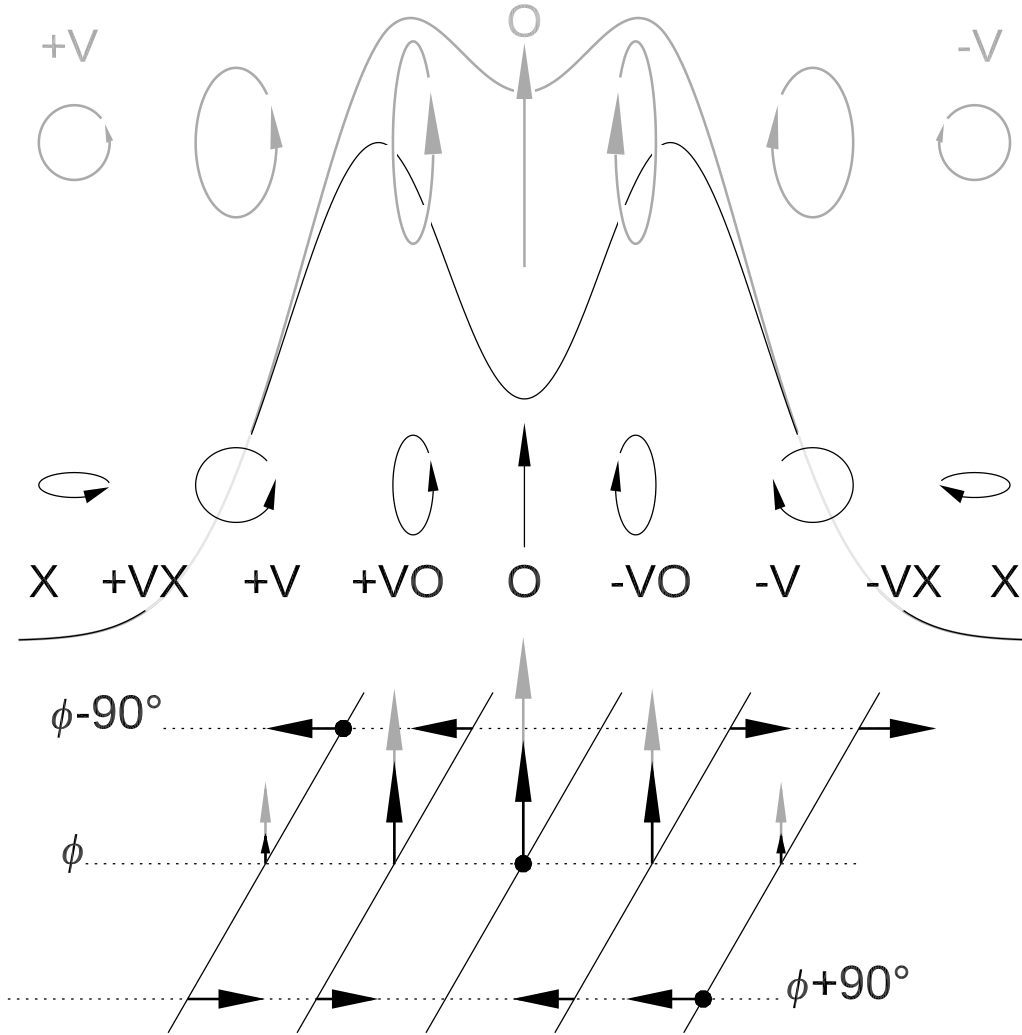


**Figure 12.** The structure of polarization and phase lags in the CR microbeam. Top grey: Polarization ellipses at different positions in the standard vacuum CR microbeam (note the opposite handedness on each side). Middle black: the ellipses for the CR beam with the suppressed O mode which leads to the meridional circularization observed in B1451-68 (sequence of polarization states: X,+V,O,-V,X). Bottom: Electric field vectors in rays that form the CR beam, shown at selected oscillation phases. The O mode suppression is shown with grey and black vertical vectors. Note the monotonic progression of the oscillation phase shown with the bullets. Black horizontal vectors (X mode) present both cases (with and without the suppression).

the ellipses on each side implies the opposite direction of the X mode vectors on each side of the microbeam (horizontal vectors in Fig. 12). Since the inversion of the vectors' direction is equivalent to the half-wave phase lag, the X mode lag indeed changes monotonously with respect to the O mode, as shown with the bullets. **This suggests that the CR microbeam is indeed buried (convolved) in the profiles of radio pulsars.**

It must be noted that the oscillations shown in Fig. 12 have been obtained by resolving the vacuum CR in two components: parallel to the B-field line plane (O mode), and orthogonal to this plane (X mode). These oscillations may seem different from the natural X and O modes of uniform magnetized plasma, which have orientation set by the  $(\vec{k}, \vec{B})$  plane, where  $\vec{k}$  is the wave vector (parallel to the line of sight). A possible physical justification for the  $\vec{B}$ -plane-governed modes involves curvature

**emission in vacuum-like conditions with the birefringence becoming efficient only at some distance from the emission point.**<sup>4</sup> The propagation of the vacuum microbeam causes the local  $\vec{B}$  field to move out of the microbeam so that the beam becomes immersed in roughly plane-parallel  $\vec{B}$ . The penetration of a birefringent region with the near-parallel  $\vec{B}$  planes would split the vacuum microbeam into the modes discussed in Fig. 12. The mechanism is thus similar (though not identical) to the adiabatic walking (Cheng & Ruderman 1979).

<sup>4</sup> Such low-density region at low altitudes reminds the polar gap.

### 6.1 The origin of subwavelength phase lags

The circular polarization  $V$  in pulsars was often interpreted in terms of the O-mode retardation (Jones 2016a; Dyks 2017), which was raising the problem of why the refraction index is so finely tuned to produce the tiny sub-wavelength phase lags (Michel 1991, p. 30). To justify the vacuum-like refraction index, the ion-proton magnetospheric plasma composition was proposed (Jones 2016b). The previous subsection shows that the subwavelength XO phase lags ( $\delta_{ox}$ ) result directly from the oscillation phase structure of the emitted CR beam. Moreover, the lag **can be** modified or produced by the scattering-driven geometric path difference. The O-mode retardation by the non-vacuum refraction index is therefore not needed to explain the observed  $V$ . **The near-vacuum refraction, on the other hand, is needed for the small phase lags to survive.**

### 6.2 Similar amount of OPMs

The NI is a very efficient process to make different amounts of OPMs similar, because the wave cancelling can be very imprecise to achieve this. The vacuum CR beam contains only 15% of the power polarized across the electron trajectory. The X/O intensity ratio of 0.15/0.85 implies the amplitude ratio of 0.39/0.92. If the O mode amplitude is reduced by just 50% (from 0.92 to 0.46) the intensity ratio of the modes becomes 0.15/0.21. **If 42% of the O-mode amplitude survives the suppression, the modes become equal.** It is thus enough for the O waves to cancel each other by more than 58% to produce MA – not a stringent condition. When the interference is cancelling less than 42% of the original amplitude, the polarization fractions can be modulated without MA (or the PA is modulated with no change of the fractions, as in the case of the coherent mode superposition at half-wave lag, ie. for  $\delta_{ox} \sim \pi + n2\pi$ , see Section 3). When  $\delta_{oo}$  is small or  $\delta_{oo} \sim n2\pi$ , the PI produces the O mode that strongly dominates in the signal.

A ubiquitous observation is the increase of polarized fractions in the minima that separate components. The overlapping adjacent components should rather depolarize each other. This effect **can result** from the scattering-driven NI, which removes the O mode while leaving the X mode behind, thus producing both the minima and the increase of polarization fraction. **However, similar effect can be caused by the Landau damping of the O mode.**

### 6.3 Why two patches?

PSR B1451–68 exhibits two antipodal patches on the P. sphere (Fig. 2 in DWI21). When staying in the QU equator, the patches can be interpreted as the linear orthogonal polarization modes (proper modes X and O). When the patches move meridionally (as in Fig. 13), they can be interpreted as a coherent mixture (superposition) of the proper polarization states (see sect. 4.1 in DWI21). This rises an interesting problem, since the coherent sum of proper modes may be expected to produce a single mixed state, whereas two states are observed.

A possible explanation is offered by Figs. 11

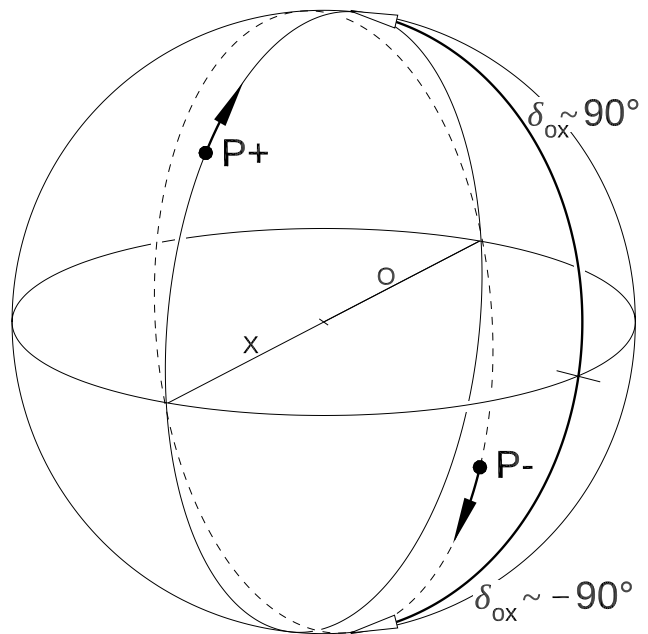


**Figure 13.** Near-meridional rotation of two polarization states ( $P+$  and  $P-$ ) on the P. sphere. If interpreted as the coherent OPM transition, The  $P+$  state is a sum of the O mode and the  $X+$  mode with a phase lag of  $+90^\circ$ . The  $P-$  state corresponds to the sum of O and  $X-$  mode with a phase lag  $-90^\circ$ . The amount of  $X+$  decreases, while the amount of  $X-$  increases in comparison to the mode O.

and 12: the CR microbeam contains the X mode-like component (the oscillation orthogonal to the  $B$  plane) which has the phase lag of opposite sign on each side of the microbeam ( $-90^\circ$  on the leading side, whereas  $+90^\circ$  on the trailing side in Fig. 12). In the following the two versions of the X mode will be called  $X-$  and  $X+$ . The coherent sum of the parallel oscillation (O mode) with the  $X+$  mode produces the positive- $V$  patch (denoted  $P+$  in Fig. 13), whereas the sum with the  $X-$  mode results in the negative- $V$  patch ( $P-$ ). The lags of  $+90^\circ$  and  $-90^\circ$  are marked with white tip arrows.

The meridional rotation is caused by variation of the mode amplitude ratio: it is interpreted as a coherent OPM jump, as described in DWI21. However, the  $P+$  patch makes the transition from the X mode to the O mode (say), while the  $P-$  patch follows the opposite way (from O to X). This implies that during the meridional rotation, the amount of the  $X+$  mode must be decreasing below the O mode, while the amount of the  $X-$  mode is increasing above the level of the O mode. This can occur at least in two situations. Firstly, when the line of sight is passing through a peak (or a minimum) of spatial emissivity, the ratio of  $X+$  and  $X-$  modes is inverted, as explained in Fig. 11. For this case to work, the amount of the O mode would have to be intermediate between the initial  $X+$  and  $X-$  modes. Secondly, the  $X+$  and  $X-$  waves are approximately coplanar and have the oscillation phase difference of  $180^\circ$ , hence they can interfere negatively

(if emission from adjacent microbeams is coherent over sufficiently large lateral scale). Such interference could produce both the azimuthal structure in the cone, and lead to the behaviour where  $X+$  is decreasing on the account of increasing amount of the  $X-$  mode. Laterally structured geometries with the X-to-O mode transition coinciding with the exchange of the X modes are possible, but the subject needs further analysis which is deferred to future work.

## 7 THE ORIGIN OF BIFURCATED COMPONENTS

The bifurcated components (BCs) can be divided in two classes: narrow conal components that merge quickly with increasing frequency ( $\Delta \propto \nu^{-1/2}$ , see fig. 6 in Dyks et al. 2007) and do not resemble the CR microbeam shape. A typical example is the trailing conal component in the millisecond PSR J0437-4715 (Navarro et al. 1997; Dai et al. 2015; Osłowski et al. 2014) although conal BCs have also been observed in normal pulsars (PSR B1946+35, Mitra & Rankin (2017), B1933+16 Mitra et al. 2016).<sup>5</sup> The other BCs are very wide precursors – the primary example is the strong and very symmetric interpulse precursor in PSR J1012+5307 (Fig. 14, based on fig. 8 in DRD10). The peaks in this BC merge with  $\nu$  at the rate  $\Delta \propto \nu^{-0.35}$  which is close to that of the CR microbeam ( $\Delta \propto \nu^{-1/3}$ ). The BC has a shape that is similar to the  $\nu$ -integrated CR microbeam.

The two BC types correspond to two different scattering regimes. The narrow fast-merging BCs are scattered within a region with small spread of velocity directions:  $\Delta \hat{v} \ll 1/\gamma_{sc}$ , where the hat means a unit vector, and  $\gamma_{sc}$  is the Lorentz factor of the scattering electrons. With no widening by the velocity spread, this implies the scattered beam size  $\Delta \sim 1/\gamma_{sc}$ . In the case of ICS, the observed frequency is roughly equal to  $\nu_{obs} \approx \gamma_{sc}^2 \nu_{em}$ , where  $\nu_{em}$  represents the peak frequency of the emitted CR spectrum. Hence  $\Delta \propto (\nu_{em}/\nu_{obs})^{1/2}$ , ie. the  $\nu$ -dependence of these BCs directly reveals the ICS origin (Dyks et al. 2007).

The strong BC in PSR J1012+5307 merges with  $\nu$  at the rate expected for CR. However, although it has been observed within a narrow frequency band of 8%, it has a shape that is very similar to the  $\nu$ -integrated CR microbeam (Fig. 14). In the  $\nu$ -resolved microbeam the intensity of CR drops steeply in the periphery (at exponential-like rate), whereas the  $\nu$ -integrated microbeam has well-developed wings, which extend far outwards. The observed  $\nu$ -resolved BC should therefore be strongly dissimilar to the  $\nu$ -integrated CR microbeam that is fitted in Fig. 14. Instead, the  $\nu$ -integrated CR beam produces a decent fit: between the dashed vertical lines  $\chi^2/\text{dof} = 3.6$  (DRD10). The strong outer wings cannot be explained by spatial convolution, because it would first remove the central minimum in the observed BC (fig. 3 in Dyks & Rudak 2013). Moreover, the BC is about ten times wider than the CR microbeam, which has

the peak separation of  $\Delta_{cr} \approx 0.8^\circ / (\nu^{1/3} \rho_{B,7}^{1/3} \sin \delta_{cut} \sin \zeta)$ , where  $\rho_B = 10^7 \text{cm} \rho_{B,7}$  is the curvature radius of electron trajectory,  $\delta_{cut}$  is the angle at which the sightline crosses the split fan beam, and  $\zeta$  is the viewing angle between the sightline and pulsar rotation axis (see fig. 2 in Dyks et al. 2012).

### 7.1 Doppler magnification

The two problems (the large width and the forbidden similarity of the  $\nu$ -resolved to the  $\nu$ -integrated beam) become solved and consistent with each other as soon as the BC originates from scattering in the regime of large spread of velocity directions ( $\Delta \hat{v} \gg 1/\gamma_{sc}$ ) and non-negligible spread of scattering electron energies ( $\gamma_{sc}$ ). If the wide low- $\nu$  CR microbeam is scattered in a region with diverging  $\vec{B}$  field (grey rectangle in Fig. 15), then each ray is directed along the black vectors of the local  $\vec{B}$ -field. Although the aberration works as usual in this scattering (sending a ray along the electron velocity), the entire original CR microbeam is not collimated (relativistically beamed) because different parts of the CR microbeam (other rays) are scattered at different magnetospheric locations by electrons moving in different directions. The beam size and shape is thus copied (ray by ray) from the low  $\nu$  to the high observed frequency  $\nu_{obs} \approx \gamma_{sc}^2 \nu$ . The spread of  $\vec{B}$  can slightly magnify the beam (by less than 3/2, as shown in Fig. 15), however, the key magnification comes from the translation in the frequency space. The beam essentially does not become wider – it is just made wider than expected at the observed  $\nu_{obs}$ , but roughly of the same size as at the much lower  $\nu$  before the scattering (see inset in Fig. 14).

### 7.2 Spectral compression

The second property – similarity to the  $\nu$ -integrated microbeam, results from the spread of the scattering electron energy. Following the gamma-square rule  $\nu_{obs} \approx \gamma_{sc}^2 \nu$ , higher-energy electrons pick up lower energies from the emitted CR spectrum, and deposit the flux at the same  $\nu_{obs}$ . The lower- $\nu$  CR is emitted in wider microbeams, which contribute predominantly to the outer wings of the observed high- $\nu$  BC. All the different CR microbeams in the emitted CR spectrum join the narrow observed band, and make the BC look  $\nu$ -integrated. Thus, the  $\nu$ -integrated shape results from the convolution of the electron energy distribution with the emitted CR spectrum (the high- $\nu_{obs}$  profile in the inset of Fig. 14 is the sum of the four inset profiles shown below).

### 7.3 Electron energies and energy budget

The BC of J1012+5307 has the 1-GHz width of about  $8^\circ$  but it may be enlarged by oblique sightline cut (small  $\delta_{cut}$ ) by unknown factor. Assuming 0.1 rad for its width, the electrons have the Lorentz factor of  $\gamma_{em} \sim 10$ , and emit very low-frequency CR at  $\nu_{cr} \approx 7 \text{ GHz} \gamma_{em}^3 / (\rho_B [\text{cm}]) \sim 1 \text{ MHz}$ . To reach the observed GHz band, the scattering electrons must have  $\gamma_{sc} \sim 30$ . This is pretty close to  $\gamma_{em} \sim 10$ , which suggests the same energy distribution for both the emitting and scattering electrons. The mechanism can thus be called the curvature-self-Compton radiation.

<sup>5</sup> It seems the bifurcations are illustrated, but not mentioned in the cited papers.

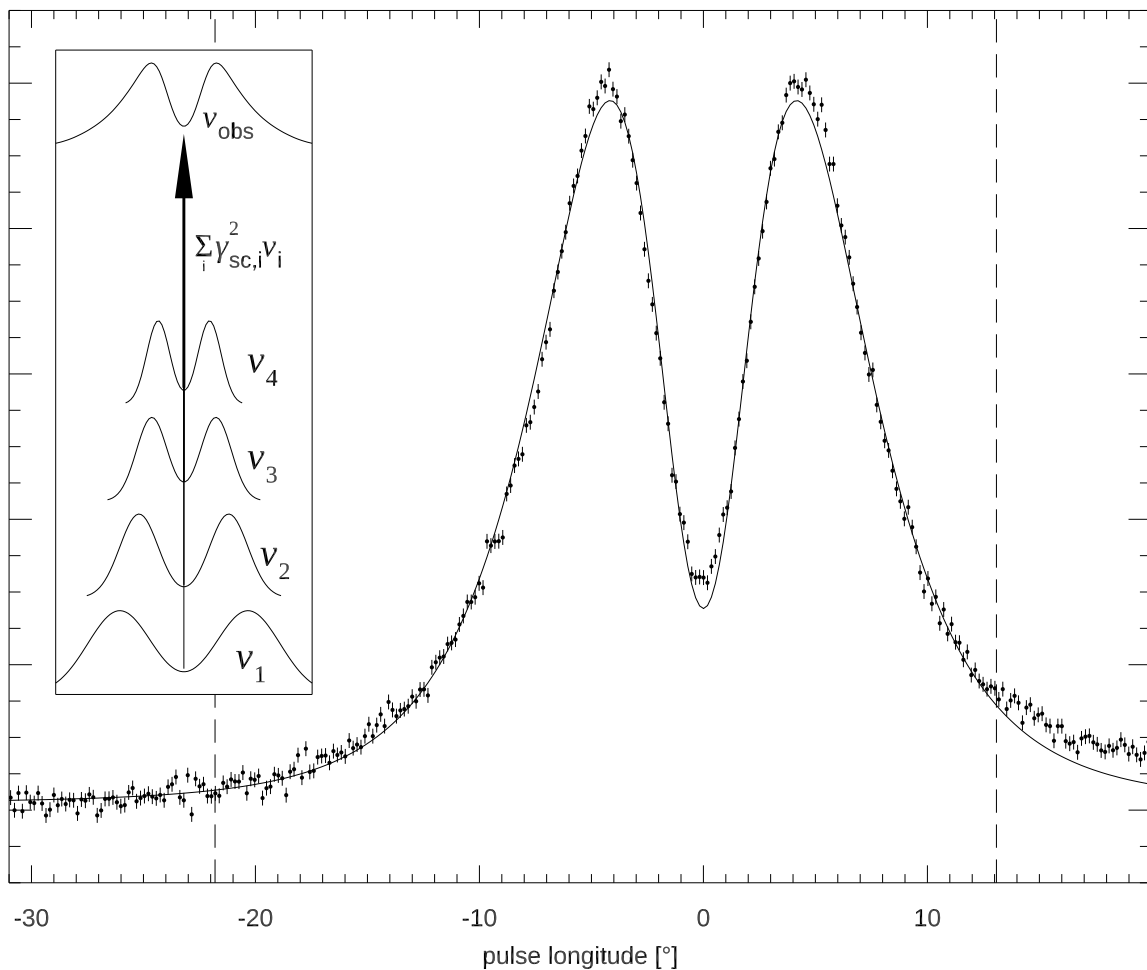


**Figure 14.** The BC in PSR J1012+5307, as observed at 0.82 GHz by GBT (from Dyks et al. 2010). In spite of the narrow bandwidth of 64 MHz (8%) the BC is well modelled by the  $\nu$ -integrated X-mode-dominated CR beam (within the dashed verticals  $\chi^2/\text{dof} = 3.6$ , error bars are statistical  $1\sigma$ , vertical scale in arbitrary units). Inset: the bright outer wings are formed by Doppler-stacking (blueshifting) of wide low- $\nu$  CR microbeams: waves of different  $\nu$  are scattered by electrons with different energy  $\gamma_{sc}$ . The large size of the low- $\nu$  microbeams is preserved by the beam-copying scattering (see next figure).

The ten-fold increase of beam size implies that the energy budget problem is abated by three orders of magnitude on account of the increased volume alone. Furthermore, the energy available within the radio band is no longer restricted by the spectral properties of the CR, since the observed BC is mostly powered by the scattering electrons. In the case of the BC of J1012+5307 the required efficiency of energy transfer to the radio band has been previously estimated as  $10^{-4}$  of the maximum power of a plasma stream, as limited by the electric potential drop and possible stream width (Dyks & Rudak 2013). Since this estimate is proportional to the stream cross-section  $A$  (see eq. 3 therein), the ten-fold increase of microbeam size decreases this power transfer efficiency to  $10^{-6}$ .

#### 7.4 Implications for subpulse modulations

The properties of bifurcated components imply that spectral effects play crucial role in determining the

observed flux of single pulse radio emission. First, the scattering must blueshift the emitted radio spectrum to reach the high frequency band normally used by radio telescopes. Second, the flux is further amplified by compressing the emitted spectrum into the narrow bandwidth used in the observations.

According to Blandford & Scharlemann (1976) the scattering ‘almost certainly’ cannot be the coherency mechanism, since scattering does not produce photons, contrary to masers. However, from the observational point of view, where flux modulations by a factor of a few make large difference, the scattering is the crucial factor, since it can move the spectrum out view, or compress the full radio spectrum into the telescope bandwidth.

As soon as the modulation phenomena are attributed to the spectral variations, it can be understood why so many of them do not involve displacement of subpulses in pulse longitude. It seems that the flux modulations have two origins: lateral rota-

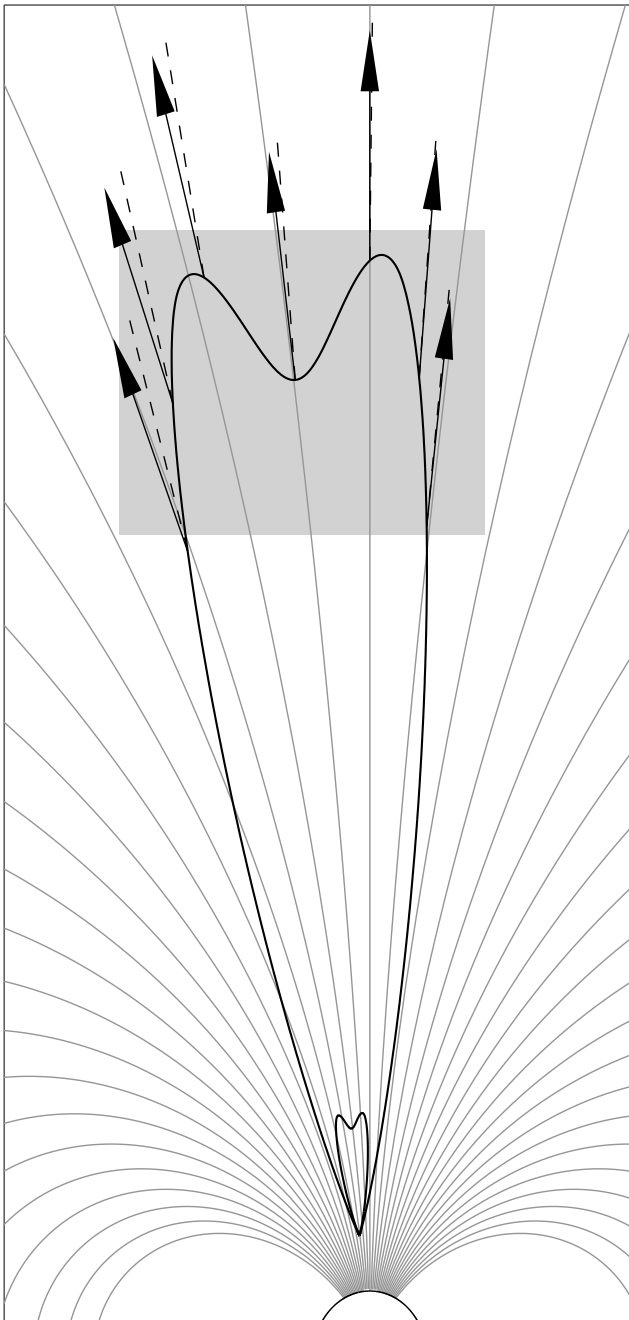


**Figure 15.** The mechanism of the ray-to-ray beam copying by scattering. Individual rays in the emitted beam (propagating along the dashed lines) are locally scattered in the direction of black arrows that represent the local velocity direction for electrons of different energy. The low- $\nu$  beam shape is thus copied to high  $\nu$  with its width slightly enlarged. The sections of dashed line are radial with respect to the emission point at bottom. Two wavefronts are shown.

tion from the  $\mathbf{E} \times \mathbf{B}$  drift and the temporal variations of the electron energy spectrum (hence of the observed radio flux and spectrum).

The spectral compression is a process in which electrons of different energy deposit different emitted frequencies at the same observed frequency (in a narrow frequency band). This may lead to in-

terference effects that affect time modulation and polarization-spectral effects as discussed in previous sections. Moreover, the production of the single-frequency wave (or the narrow frequency band) from the entire radio spectrum involves coherent wave superposition, which looks like a process that may be responsible for the coherent amplification itself. However, for the scattering process to start operating the optical path for scattering must be sufficiently high, which, according to the above-cited literature, requires the initial CR emission to be already amplified.

### 7.5 Bifurcations of conal components

The BCs have been considered as the main justification for the nonconal beam geometry (system of radial fan beams, see fig. 18 in DRD10), because the diverging plasma flow in the polar region was expected to smear any structure in latitude (fig. 1 in Dyks 2017a). For the bifurcation of conals to be possible, the corotation of the magnetosphere must break the symmetry centred on the dipole axis. Moreover, for the scattering to be possible, the orthogonal polarization of the X mode must be transformed into the parallel polarization, which can also be enabled by the corotation. A simplified geometric analysis of this effect is presented in the Appendix. Alternatively, orthogonal modes of scattering may operate in finite magnetic field (Petrova 2008b).

## 8 DISCUSSION

The proposed processes are likely responsible for many other interesting effects observed in radio pulsars.

The 16-millisecond PSR J1022+1001 exhibits displaced PA curve (fig. 8 in Ramachandran & Kramer 2003) with ‘unstable’ components and frequency evolution which follows the pattern shown in Fig. 7. The phenomenon has been tentatively interpreted as the effect of return currents that distort the local  $B$  field (Hibschmann & Arons 2001). It is suggested here that the profile evolution (and unstable character of emission) results from the scattering. With increasing  $\nu$  the MFP becomes shorter than the size of the magnetosphere, so the profile develops strong conal components that are subsequently, i.e. with further decrease of MFP, contracted to the narrow single peak (fig. 1 therein). The main difference from Fig. 7 is that the profile of this fast-rotating pulsar is made asymmetric by the corotation effects.

The high-frequency interpulse and the high-frequency components in the Crab pulsar (Moffett & Hankins 1996; 1999) also reveal clear features of scattering (Petrova 2009). They appear at shifted longitude but do not move much with  $\nu$ , and have a flat PA curve with the interpulse showing the MA between 1.4 and 5 GHz. The striped spectrum of the interpulse has already been considered as a possible effect of interference (Eilek & Hankins 2016) which is in line with the effects of ray redirection and Doppler-stacking described in this paper.

The flat PA curve in fast radio bursts (FRBs, Day et

al. 2020; Price et al. 2019) as well as their large energy requirements are very similar to the properties of radio pulsar signals. It is therefore tempting to suggest similar mechanisms to explain FRBs. If FRBs result from scattering that leads to coherent interference with MA in time domain, the MA can produce false impression of variable rotation measure (Hilmarsson et al. 2020). This is because in case of coherent mode summation, the variable mode amount ratio can be observed as the rotation of polarization direction (Fig. 4). Moreover, the defocusing (magnifying) properties of pulsar magnetosphere raise the question on whether an opposite effect is also possible: focusing of rays by scattering in the ray-to-ray beam-copying mode. This is essentially equivalent to the question: does the propagation-related flux decrease (that follows the  $1/r^2$  rule) apply to all observed astronomical signals? Can a weak focusing result in caustic amplification of signals at far distance from the emitting source?

## 9 CONCLUSIONS

I have shown that geometric properties of radio pulsar signals provide **important** information on their physics. The proposed **interpretation of radio signals** involves several new effects, such as the coherent OPM transitions that are undetectable in polarized fractions, the preference of long-MFP scattering into cones, the negative interference of the scattered rays with the ensuing mode alternation in time and  $\nu$ , the CR-microbeam-driven circular polarization (which does not require the subwavelength O-mode retardation by the slightly non-vacuum refraction index), the transport of microbeams in the frequency space, with their width roughly preserved **and the spectral compression to the telescope bandwidth**. To observe the radio flux at a high  $\nu$  (ie. around normally observed 1 GHz) the original CR emission must pass through scattering-favorable regions of magnetosphere (**with appropriate electron energy distribution**), and furthermore must be sent towards a radio telescope. The shape of pulse profile at a given  $\nu$  (and modulation pattern) thus strongly depends on whether the waves can be upshifted to the observed band.

This work **suggests** that circular polarization in pulsars originates from the intrinsic properties of the CR microbeam, and from the coherent superposition of scattered waves. The small phase lags needed to explain the observed  $V$  thus result from the geometric path difference and from the intrinsic properties of CR. The **finely-tuned** refraction index is not necessary to produce the subwavelength phase lags. **However, a near-vacuum refraction index is anyway needed for the circular polarization to survive.**

The ICS in pulsar magnetosphere causes multiple imaging and magnifies the view of the CR emission: both through the divergency of  $B$ -field (cones are an enlarged image of core) and through the Doppler-magnification of the BCs, which makes the microphysics of CR so strikingly visible.

The finite (not negligible) width of the emitted elementary radiation pattern is important to understand the properties of radio pulsar signals. The microbeam width is much larger than expected, because the observed frequency cannot be directly interpreted in terms of the curvature spectrum. The ICS-induced Doppler shift implies that CR microbeams

are several (up to ten) times larger than previously thought. This makes them comparable to the flaring of the polar tube, which abates the energy requirements by orders of magnitude.

The results show **that polarization data involve numerous OPM transitions that can be interpreted as the result of** the coherent mode superposition. The OPM transitions are therefore undetectable in the polarized fractions. The PA tracks are distorted because scattering is displacing rays in longitude, and because of the coherent mode superposition (stairs-shaped PA curves). This has important practical consequences for the RVM fitting.

The overlapping O-mode waves can be cancelled by the negative interference (or amplified by the PI) which has important implications for modulation studies. Effects of the time-dependent interference naturally lead to the OPM alternation and provide more flexible model than the carousel of sparks. The model based on intrabeam interference is also capable of producing the half-wave lag which so far was interpreted through surface oscillations. **It must be emphasized, however, that the time modulations do not exclude the slow lateral rotation caused by the ExB drift. Moreover, the modulation is certainly affected by the spectral effects of blueshift and compression into a narrow bandwidth.**

The interference-driven mode alternation can produce gradual changes of PA in frequency and time, if the coherent sum of the modes is observed. This can affect rotation measure determinations and the correlation of the specific polarization mode with the proper motion direction.

It has been shown that pulsar profiles indeed **seem to** have conal properties, however, the cones must unavoidably be structured in azimuth because of the corotation effects, and likely because of azimuthal interference effects. The agreement between the observed and theoretical cone ratio implies that pulsar magnetosphere is indeed dipolar in the radio emission region (which extends between the emission and scattering altitudes).

Two emission mechanisms: the curvature radiation and the inverse Compton mechanism, **appear to** take place in radio pulsars. The radiative processes can together be called the curvature-self-Compton radiation.

**It has been shown that the observed geometry of radio pulsar signals gives considerable insight into the physics of radio pulsar signals.** With the multiple imaging, Doppler microbeam magnification, **spectral compression**, coherent mode transitions and interference-driven wave cancelling, the pulsar magnetosphere emerges as an astonishing astrophysical environment.

## ACKNOWLEDGMENTS

I thank Simon Johnston for Fig. 2 and Bronek Rudak for comments on the manuscript. This work was supported by the grant 2017/25/B/ST9/00385 of the National Science Centre, Poland.

**DATA AVAILABILITY STATEMENT**

The data for J1012+5307 are available from the author on request and with permission of Paul Demorest.

**REFERENCES**

- Blandford R. D., Scharlemann E. T., 1976, *MNRAS*, 174, 59
- Blaskiewicz M., Cordes J. M., Wasserman I., 1991, *ApJ*, 370, 643
- Cheng A. F., Ruderman M. A., 1979, *ApJ*, 229, 348
- Clemens J. C., Rosen R., 2004, *ApJ*, 609, 340
- Clemens J. C., Rosen R., 2008, *ApJ*, 680, 664
- Dai S., Hobbs G., Manchester R. N., Kerr M., Shannon R. M., van Straten W., Mata A., Bailes M., Bhat N. D. R., et al., 2015, *MNRAS*, 449, 3223
- Day C. K., Deller A. T., Shannon R. M., Qiu H., Bannister K. W., Bhandari S., Ekers R., Flynn C., James C. W., Macquart J.-P., Mahony E. K., Phillips C. J., Xavier Prochaska J., 2020, *MNRAS*, 497, 3335
- Deshpande A. A., Rankin J. M., 2001, *MNRAS*, 322, 438
- Desvignes G., Kramer M., Lee K., van Leeuwen J., Stairs I., Jessner A., Cognard I., Kasian L., Lyne A., Stappers B. W., 2019, *Science*, 365, 1013
- Dyks J., 2017a, *MNRAS*, 471, L131
- Dyks J., 2017b, *MNRAS*, 472, 4617
- Dyks J., 2019, *MNRAS*, 488, 2018
- Dyks J., 2020, *MNRAS*, 495, L118
- Dyks J., Pierbattista M., 2015, *MNRAS*, 454, 2216
- Dyks J., Rudak B., 2012, *MNRAS*, 420, 3403 (DR12)
- Dyks J., Rudak B., 2013, *MNRAS*, 434, 3061
- Dyks J., Rudak B., Demorest P., 2010, *MNRAS*, 401, 1781
- Dyks J., Rudak B., Rankin J. M., 2007, *A&A*, 465, 981
- Dyks J., Weltevrede P., Ilie C., 2021, *MNRAS*, 501, 2156 (DWI21)
- Dyks J., Wright G. A. E., Demorest P., 2010, *MNRAS*, 405, 509
- Edwards R. T., Stappers B. W., 2004, *A&A*, 421, 681
- Edwards R. T., Stappers B. W., van Leeuwen A. G. J., 2003, *A&A*, 402, 321
- Eilek J. A., Hankins T. H., 2016, *Journal of Plasma Physics*, 82, 635820302
- Esamdin A., Lyne A. G., Graham-Smith F., Kramer M., Manchester R. N., Wu X., 2005, *MNRAS*, 356, 59
- Galishnikova A. K., Philippov A. A., Beskin V. S., 2020, *arXiv e-prints*, p. arXiv:2008.13750
- Gangadhara R. T., 2010, *ApJ*, 710, 29
- Gil J., Lyubarsky Y., Melikidze G. I., 2004, *ApJ*, 600, 872
- Gil J., Melikidze G. I., Geppert U., 2003, *A&A*, 407, 315
- Gupta Y., Gil J., Kijak J., Sendyk M., 2004, *A&A*, 426, 229
- Hakobyan H. L., Beskin V. S., Philippov A. A., 2017, *MNRAS*, 469, 2704
- Hankins T. H., Rankin J. M., 2010, *AJ*, 139, 168
- Hankins T. H., Wright G. A. E., 1980, *Nat*, 288, 681
- Hibschman J. A., Arons J., 2001, *ApJ*, 546, 382
- Hilmarsson G. H., Michilli D., Spitler L. G., Wharton R. S., Demorest P., Desvignes G., Gourdji K., Hackstein S., Hessels J. W. T., Nimmo K., Seymour A. D., Kramer M., McKinven R., 2020, *arXiv e-prints*, p. arXiv:2009.12135
- Ilie C. D., 2019, PhD Thesis, The University of Manchester
- Johnston S., Hobbs G., Vigeland S., Kramer M., Weisberg J. M., Lyne A. G., 2005, *MNRAS*, 364, 1397
- Johnston S., Karastergiou A., Mitra D., Gupta Y., 2008, *MNRAS*, 388, 261
- Jones P. B., 2016a, *MNRAS*, 455, 3814
- Jones P. B., 2016b, *MNRAS*, 459, 3307
- Kaganovich A., Lyubarsky Y., 2010, *ApJ*, 721, 1164
- Karastergiou A., 2009, *MNRAS*, 392, L60
- Kramer M., Wielebinski R., Jessner A., Gil J. A., Seiradakis J. H., 1994, *A&AS*, 107, 515
- Luo Q., Melrose D. B., 1992, *MNRAS*, 258, 616
- Lyubarskii Y. E., Petrova S. A., 1996, *Astronomy Letters*, 22, 399
- Lyubarskii Y. E., Petrova S. A., 1998, *Astrophysics and Space Science*, 262, 379
- Maan Y., 2019, *ApJ*, 870, 110
- McLaughlin M. A., Rankin J. M., 2004, *MNRAS*, 351, 808
- McSweeney S. J., Bhat N. D. R., Wright G., Tremblay S. E., Kudale S., 2019, *ApJ*, 883, 28
- Melrose D., 2003, in Bailes M., Nice D. J., Thorsett S. E., eds, *Radio Pulsars Vol. 302 of Astronomical Society of the Pacific Conference Series, What Causes the Circular Polarization in Pulsars?*. p. 179
- Melrose D., Miller A., Karastergiou A., Luo Q., 2006, *MNRAS*, 365, 638
- Michel F. C., 1991, *Theory of neutron star magnetospheres*. University of Chicago Press
- Mitra D., Deshpande A. A., 1999, *A&A*, 346, 906
- Mitra D., Gil J., Melikidze G. I., 2009, *ApJ*, 696, L141
- Mitra D., Rankin J., 2017, *MNRAS*, 468, 4601
- Mitra D., Rankin J., Arjunwadkar M., 2016, *MNRAS*, 460, 3063
- Mitra D., Rankin J. M., 2008, *MNRAS*, 385, 606
- Moffett D. A., Hankins T. H., 1996, *ApJ*, 468, 779
- Moffett D. A., Hankins T. H., 1999, *ApJ*, 522, 1046
- Navarro J., Manchester R. N., Sandhu J. S., Kulkarni S. R., Bailes M., 1997, *ApJ*, 486, 1019
- Ng C., Pandhi A., Naidu A., Fonseca E., Kaspi V. M., Masui K. W., Mckinven R., Renard A., Scholz P., Stairs I. H., Tendulkar S. P., Vand erlinde K., 2020, *MNRAS*, 496, 2836
- Noutsos A., Sobey C., Kondratiev V. I., Weltevrede P., Verbiest J. P. W., Karastergiou A., Kramer M., et al. 2015, *A&A*, 576, A62
- Osłowski S., van Straten W., Bailes M., Jameson A., Hobbs G., 2014, *MNRAS*, 441, 3148
- Petrova S. A., 2004, *A&A*, 424, 227
- Petrova S. A., 2006, *MNRAS*, 366, 1539
- Petrova S. A., 2008a, *MNRAS*, 384, L1
- Petrova S. A., 2008b, *ApJ*, 673, 400
- Petrova S. A., 2009, *MNRAS*, 395, 1723
- Price D. C., Foster G., Geyer M., van Straten W., Gajjar V., Hellbourg G., Karastergiou A., Keane E. F., Siemion A. P. V., Arcavi I., Bhat R., et al. 2019, *MNRAS*, 486, 3636
- Ramachandran R., Kramer M., 2003, *A&A*, 407, 1085
- Rankin J. M., 1983, *ApJ*, 274, 333
- Rankin J. M., 1988, *ApJ*, 325, 314
- Rankin J. M., 1993, *ApJ*, 405, 285
- Ruderman M. A., Sutherland P. G., 1975, *ApJ*, 196, 51
- Smith E., Rankin J., Mitra D., 2013, *MNRAS*, 435, 2002
- Sokolov A. A., Ternov I. M., 1968, *Synchrotron Radiation*. New York: Pergamon
- Srostlik Z., Rankin J. M., 2005, *MNRAS*, 362, 1121
- Stinebring D. R., Cordes J. M., Rankin J. M., Weisberg J. M., Boriakoff V., 1984, *ApJS*, 55, 247
- Tiburzi C., Johnston S., Bailes M., Bates S. D., Bhat N. D. R., Burgay M., Burke-Spolaor S., Champion D., Coster P., D'Amico N., et al., 2013, *MNRAS*, 436, 3557
- Wang C., Lai D., Han J., 2010, *MNRAS*, 403, 569
- Wang P. F., Wang C., Han J. L., 2015, *MNRAS*, 448, 771
- Weltevrede P., Stappers B. W., Edwards R. T., 2007, *A&A*, 469, 607
- Wright G. A. E., 2003, *MNRAS*, 344, 1041
- Young S. A. E., Rankin J. M., 2012, *MNRAS*, 424, 2477

## APPENDIX: BIFURCATIONS OF CONAL COMPONENTS IN THE PRESENCE OF COROTATIONAL ASYMMETRY

The model discussed here assumes that the CR microbeam consists of only the bifurcated X mode part and is polarized mostly orthogonally to the plane of the B field curvature (Gil et al. 2004). The propagation of polarized waves in magnetized plasma (Petrova 2006; Wang et al. 2010) is here extremely simplified. Only two altitudes are considered: the emission altitude (low) and the scattering altitude (high). It is assumed that the adiabatic walking (AW) of polarization direction (Cheng & Ruderman 1979) does not occur and the rays avoid Landau absorption before the scattering. Only the oscillations parallel to B planes are scattered, ie. the perpendicular modes of scattering are ignored (Blandford & Scharlemann 1976).

As can be seen in Fig. 10, during the upward propagation of the CR beam, the magnetic axis moves out of the beam. Based on Fig. 10 it may seem that the dipole axis moves left, ie. to the leading side of the magnetosphere, however, considering the axis as the least curved electron trajectory in the observer reference frame, it may be inferred from Fig. 10, that the axis moves rightward, ie. to the trailing side (Blaskiewicz et al. 1991). As can be seen in Fig. 10, the photons emitted on the trailing side propagate roughly along the dipolar magnetic field in the corotating frame. Given almost the same speed of electrons and photons, this means that trailing side electrons move rectilinearly in the inertial observer frame, just as the photons do (see fig. 2 in Dyks, Wright & Demorest 2010). Thus the dipole axis moves right because of the straightening of electron trajectories in the inertial observer frame, which occurs on the trailing side of the magnetosphere.

The rotational breaking of symmetry implies that even the conal pulsar beams *have to be* structured in azimuth. **Since the following geometric considerations only rely on the relative orientation of the microbeam polarization and the local magnetic field, they also apply to other pulsar beams, including a uniform beam or a set of fan beams.**

In Fig. 16 the low-altitude B-field is shown with thick grey lines that spread radially from the low altitude dipole axis (LAP stands for low-altitude pole). The X mode polarization direction is orthogonal to this low- $r$  B-field, as shown with the white arrows. The high altitude B-field is shown with thin lines that emerge from the high-altitude pole (HAP) on the right. While propagating upwards in the absence of AW, the bifurcated X mode part of the CR microbeam can be oriented in such way that its polarization is parallel to the local B plane at large  $r$ . This happens at point P in Fig. 16, where the full originally-X mode beam can be scattered in the form of the O-mode rays.

### Azimuthal beam structure and survival of bifurcations

The same parallel orientation of the X mode polarization occurs for any point at the thick solid circle that passes through both poles (LAP and HAP). This mode-redefining

circle is made of points at which the low- $r$  field is orthogonal to the high- $r$  field, and it is given by the equations:

$$\theta_x = \theta_{\text{DA}} \cos^2 \phi_{\text{lr}} \quad \theta_y = \theta_{\text{DA}} \cos \phi_{\text{lr}} \sin \phi_{\text{lr}}, \quad (4)$$

where  $\theta_{\text{DA}}$  is the angular misalignment between the low- $r$  and high- $r$  magnetic field structure,  $\phi_{\text{lr}}$  is the azimuth measured around the low- $r$  magnetic dipole axis.

Fig. 16 shows only selected bifurcated microbeams, in a beam which may have uniform emissivity that fills in the entire surface of the figure. If the scattering occurs for oscillations parallel to the high- $r$  magnetic field, only the parallel-polarized parts of the microbeams can be scattered. Therefore, in the following I discuss only such O-mode-like parts of the X-mode microbeams. The projections of the originally-orthogonal polarization on the direction parallel to the high- $r$  B field are shown for points K and L in Fig. 16. The magnitude of the projections decreases with distance from the thick circle.

**The microbeams scattered at the thick solid circle will be relocated to the dotted circle, which is larger by a factor of 1.5. In particular, scattering of radiation near point P will move the P microbeam to position N, as results from the 3/2 rule (and the microbeam will be Doppler shifted to a higher  $\nu$ ). The eight microbeams that are plotted in Fig. 16 will also form an enlarged ring (cone). For example, the K point on the left side is far from HAP, so it will be scattered at a large angle. Therefore, a rescaled set of scattered microbeams should be discussed below. However, for brevity (to avoid another figure showing the scattered beam) I will discuss the emitted microbeams shown in Fig. 16, assuming that their part polarized orthogonally to the high- $r$   $\vec{B}$  is missing (since it cannot be scattered to the observation band).<sup>6</sup>**

Even for uniform beam emissivity, the passage of sight-line through the point N (scattered from P) will produce a BC, because radiative contributions of bifurcated neighboring microbeams decrease with distance from the thick-line circle. This can be shown even for emissivity that is uniform in the low- $r$  azimuth (measured around LAP). Consider another two bifurcated microbeams at positions A and B in Fig. 16 (the microbeams are not shown). One lobe in each microbeam contributes at point P thus increasing the flux at the central minimum in the BC observed at point N(P). However, this fill-up is not complete for the following reason. The projection of the X mode polarization direction on the high- $r$  B-field decreases with distance from the thick-line circle, as shown at points K and L. Therefore, the X mode radiation from points A and B cannot fully fill in the central minimum in the BC at point P. It is because the polarization of the A and B microbeams is slightly twisted with respect to that at point P, so they cannot contribute their full radiative energy at P. The intensity of the originally-X mode radiation that can become the upscattered O mode, decreases with distance from the thick-line circle. **The solid circle thus marks the possible location of double notches, whereas the dotted circle – the position of BCs.**

Near the centre of Fig. 16, the high- $r$  B field is almost

<sup>6</sup> Constraining the scattering to the parallel-polarized waves may be released if the scatterings occur at high altitudes in weak B.

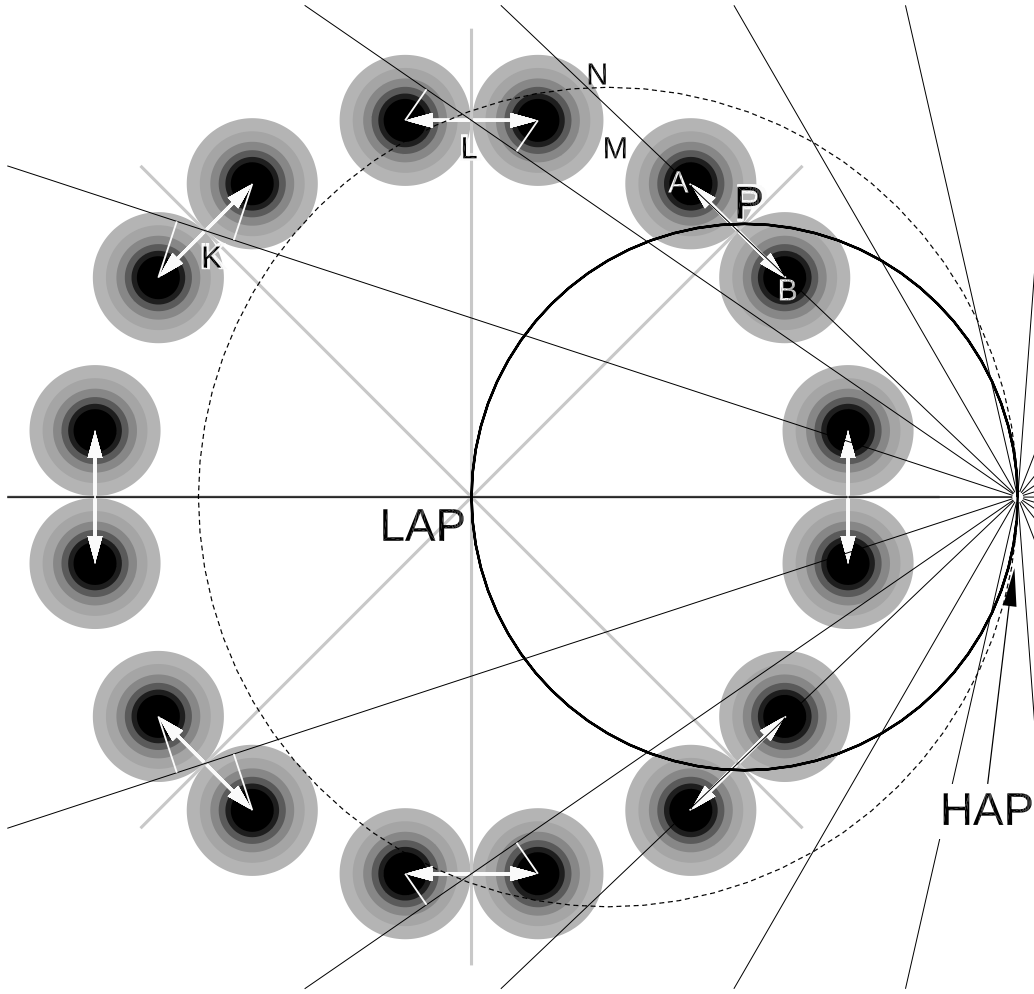


**Figure 16.** Polarization of X-mode part of CR microbeams in  $B$ -field at two different altitudes. Thin solid lines show the high- $r$  magnetic field. The high- $r$  dipole axis (viewed head-on, and located near the right margin) is displaced out of the beam. Only selected microbeams are shown. They are two-lobed and polarized along the white arrows, ie. across the low- $r$   $B$ -field shown with thick grey lines. At point P the entire X-mode microbeam can be scattered, because the upward propagation makes its pol. direction parallel to the high- $r$   $B$ . The same holds along the thick solid circle. **Microbeams scattered at the solid circle are relocated to the dotted circle.**

horizontal, therefore, the mode-redefining circle is passing near-vertically through the low- $r$  beam centre. The bifurcated X-mode microbeams emitted near the main meridional plane (that contains the rotation axis and the low- $r$  dipole axis) are therefore polarized along the high-altitude O-mode direction and can be upscattered as the O-mode rays. This **may produce** the bifurcation of core components (observed eg. in J0437-4715, Navarro et al. 1997).

With no adiabatic walking or dumping, the propagation-related twist of the the local, ie. high- $r$   $B$  field (with respect to the original X mode polarization direction) can thus result in rays having the polarization parallel to  $\vec{B}$ , so that the rays can be scattered as the O mode. As shown in Fig. 16, the relative amount of the fresh-O and the still-X mode is changing with the low- $r$  azimuth (beam-centred azimuth). **Under the assumed conditions** all the observed O-mode radiation **could have the X-mode origin**: the originally emitted low-altitude CR does not have to contain the O mode at all: it can be pure X mode emission. This way of O-mode creation is consistent with the

observed similar amount of X and O modes. Moreover, the initially-orthogonal polarization **may allow** for the upward propagation of the X mode microbeams in the lower magnetosphere, so that different rays from the same microbeam can propagate through different magnetospheric locations at high  $r$ .

The non-negligible size of the emitted X mode microbeams implies possible interference between their X mode waves, which can produce additional azimuthal structure in the azimuthal direction. The X-mode-like polarized rays on each side of the CR microbeam have the relative phase lag of  $180^\circ$  (Fig. 12), which favors wave cancelling even with no additional processes (like scattering) involved. Therefore, the X mode flux can be cancelled by the NI, if the lateral scale of coherency is sufficiently large.

**BCs versus double notches.**

The bifurcated beam at P in Fig. 16 can be scattered to the location N which is  $3/2$  times further from the high- $r$  pole (if MFP is long). The scattering removes the two lobes (near points A and B) of the bifurcated beam at P. The removed flux can be observed as double notches in pulse profiles (McLaughlin & Rankin 2004). The same reasoning can be applied for any point along the solid mode-redefining circle: **if the scattering occurs over a sufficiently wide band, double notches can be observed at longitudes where our sightline is cutting through the solid circle. The BCs can be detected near the dotted circle.** In J0437-4715 the notches are indeed observed in the trailing wing of a trailing-side BC (Navarro et al. 1997). The observed double notches have steep exponential-like outer wings, consistent with the  $\nu$ -resolved CR beam (fig. 6 in Dyks & Rudak 2012). **Thus, it seems that** the scattering is carving out double notches observed at a different  $\nu$  and stacking them in a narrow-band BC observed at a higher  $\nu$  and different  $\Phi$ .